Journal of
Materials Chemistry A

ROYAL SOCIETY
OF CHEMISTRY

PAPER

View Article Online
View Journal | View Issue

Check for updates

Cite this: J. Mater. Chem. A, 2025, 13, 29431

Hydride synthesis of thermoelectric skutterudites (Ba,Sr)$Fe_{3\pm x}Ni_{1\pm x}Sb_{12}$ optimized *via* design of experiments†

Thomas A. Seymour-Cozzini, Rae A. Earnest ‡ and Julia V. Zaikina *

Received 26th April 2025
Accepted 19th July 2025

DOI: 10.1039/d5ta03288a

rsc.li/materials-a

Reactive metal hydrides, SrH_2 and BaH_2, were used to make the novel thermoelectric skutterudite $Sr_{0.92}Fe_{2.98\pm x}Ni_{1.00\pm x}Sb_{12}$ and the previously studied skutterudite $Ba_{0.9}Fe_{3.00\pm x}Ni_{1.00\pm x}Sb_{12}$, demonstrating the advantages of the diffusion-enhanced hydride synthesis. High-temperature *in situ* powder X-ray diffraction showed that BaH_2, Fe, Ni, and Sb react to form binary and pseudo-binary intermediate products, which further react with one another and the remaining Sb to form $BaFe_3NiSb_{12}$ in a narrow temperature range around 855 K, the optimal synthesis temperature of $BaFe_3NiSb_{12}$. Statistical analysis, the fundamental basis of design of experiments (DoE) methodology, was tested using 12 synthesis attempts, and indicated 861 K was the optimal annealing temperature for $BaFe_3NiSb_{12}$ synthesis, validating the utility of statistical methods for the optimization of synthesis conditions in multicomponent solid-state systems. Synthesis optimization for $SrFe_3NiSb_{12}$ was performed entirely using DoE tools, demonstrating the efficacy of DoE to narrow down the set of conditions needed to form single-phase products using the fast hydride route. Synthetic insensitivity to the ratio of Fe to Ni enabled tuning of electronic transport properties, resulting in a peak thermoelectric figure of merit (zT) of 0.54 at 673 K for $Sr_{0.92}Fe_{3.28}Ni_{0.70}Sb_{12}$.

Introduction

The increasing societal demand for electrical energy must be met with wider use of renewable energy sources and more efficient energy conversion, storage, and transmission. Lawrence-Livermore National Laboratory and the U.S. Department of Energy estimate that approximately 2/3 of energy production is wasted as unused heat.[1] Thermoelectric generators present a viable option to recover wasted heat by converting heat flow into usable electrical energy. The thermoelectric generator offers greater reliability than other heat engines due to the lack of moving parts; its service life is limited by the chemical stability of the thermoelectric materials used in its construction and not by mechanical wear. Thermoelectric power conversion has been used since the 1940s to power electrical equipment under inhospitable conditions where a small continuous heat source is the only viable source of power,[2] exemplified by the thermoelectrically powered Voyager missions,[3] the longest-lived space probes to date.

The heat conversion efficiency of a thermoelectric material increases with an increasing figure of merit, zT, which is calculated based on the absolute temperature, T, Seebeck coefficient, S, thermal conductivity, κ, and electrical resistivity, ρ, according to the equation$zT = \frac{S^2}{\rho\kappa}T$. Therefore, the ideal thermoelectric material has low thermal conductivity, low electrical resistivity, and a high Seebeck coefficient, maximizing zT.[4,5] The Seebeck coefficient, electrical resistivity, and thermal conductivity are all related to the charge carrier concentration in a given material. This interdependence makes the optimization of zT difficult. Recent leaps in materials design have seen zT double[6] over previous state-of-the-art materials, increasing from 1 to approximately 2. This is much closer to the zT of 3 expected to make thermoelectric materials a commercially viable means of electrical power generation.[7] Advances in caged materials made since 1995 largely stem from Slack's phonon-glass electron-crystal concept,[8] which decouples lattice thermal conductivity from the electrical properties of a thermoelectric material. A phonon-glass electron-crystal is a hypothetical material that can scatter thermal phonons effectively as if it is amorphous (glass) but can also conduct electricity well as if it is crystalline.[8] Attempts to realize this decoupling of electrical and thermal properties are most successful in compounds with cage motifs in their crystal structure. Filled skutterudites with the $LaFe_4Sb_{12}$ structure type are one example of a phonon-glass electron-crystal material. Filled skutterudites have a cubic

---

Department of Chemistry, Iowa State University, Ames, Iowa 50011, USA. E-mail: yzaikina@iastate.edu

† Electronic supplementary information (ESI) available. See DOI: https://doi.org/10.1039/d5ta03288a

‡ Present Address: Department of Chemistry, University of Utah, Salt Lake City, Utah 84112, USA.

framework of late transition metals, typically Fe or Co, in distorted octahedral coordination by pnictogen atoms, typically Sb, where each pnictogen atom also bonds to adjacent pnictogen atoms.[9] A "rattler" atom occupies the large void at the origin of the body-centered unit cell (space group $Im\bar{3}$ No. 204).[9,10] The rigid, covalently bonded framework provides a robust, conductive skeleton needed to satisfy the requirements of an electron crystal, and the large thermal displacement parameters of caged rattler atoms allow them to scatter heat-carrying phonons, decreasing thermal conductivity as in a phonon glass.[11–14]

Skutterudites with high zT are typically n-type semiconductors with multiple types of filler atoms and a Co–Sb framework.[11] The p-type skutterudites also show excellent performance with zT values above 1. High-performance p-type skutterudites typically have a framework of Fe, Co, and Sb with a combination of lanthanide fillers (La–Nd, Gd, Yb).[11,12] Using a substantial number of literature examples,[11] one finds the best performing p-type skutterudites have a valence electron count (VEC) for one formula unit between 71.5 and 72. Applying this electron counting formalism to $LaFe_4Sb_{12}$, which contains one La^{3+} ion donating three electrons, four $4s^23d^6$ Fe atoms, and twelve $5p^3$ Sb atoms results in a VEC of $1(3) + 4(8) + 12(3) = 71$. Only electrons at the top of the valence band are accounted for, thus determining the position of the Fermi level, hence, Sb contributes 3 electrons to the count and not 5.[11–15] The Sb $5s^2$ electrons states are part of the valence band but are much lower in energy than the Fermi level.

Using the Zintl–Klemm formalism[16,17] and considering that each Sb atom has bonding interactions with two other Sb atoms in the skutterudite structure (Sb–Sb distances ≈ 3 Å), the following Zintl charges can be assigned: $(La^{+3})(Fe^{+2})_4(Sb^{-1})_{12}$, 1 electron away from charge-balanced composition, consistent with VEC = 71, not 72. For a transition metal (Fe) in an octahedral ligand field of Sb ligands, the low-spin d^6 state is the most stable. This makes the replacement of Fe ($4s^23d^6$) with Co ($4s^23d^7$) or Ni ($4s^23d^8$) a viable means of electron-doping to retain the favorable electronic properties of the parent "unfilled" $CoSb_3 \equiv (Co^{+3})_4(Sb^{-1})_{12}$ skutterudite. Doping Co (or Ni) into Fe sites allows one to adjust the position of the Fermi level and to tune carrier concentrations for optimal electronic transport properties. Although most p-type filled skutterudites with high zT values use Fe and Co frameworks to retain a nearly optimal VEC, some examples do use Fe and Ni. These Ni-containing filled skutterudites have also shown comparable zTs of 1 or more,[11–15] but there are far fewer examples of them in literature despite ongoing ethical and geopolitical concerns over the use of cobalt.[9,11,18]

Design-of-experiments (DoE) tools are commercially available software that use statistical models to map the effects of individual parameters on the outcome of any complex process. With planning, these models are more thorough than the mental picture assembled by a human experimenter who can only track changes made to one variable per experiment.[19] By enabling an experimentalist to change more than one variable at a time while exploring multinary phase space,[20] statistical design of experiments techniques can vastly decrease the number of attempts needed to find true optima in a given synthetic system.[21] By deconvoluting the effects of synthetic variables, one can more fully understand which aspects of a synthetic system are most important to achieving the desired outcome.[22–24] Despite the powerful analytical advantages afforded by DoE, its applicability has limits. If an experimenter's intuition can lead to desirable results in fewer trials than DoE requires to model a synthetic system, there is little reason to adopt statistical analysis. This is especially true if the synthesis in question is so expensive or slow that a total of 20 to 30 optimization attempts is impractical.

As such, traditional "heat-n-beat" solid-state synthesis is often unsuitable for statistical DoE. For example, skutterudite synthesis takes about a week by traditional solid-state methods, with two separate heating steps and intermediate regrinding.[10–15,25–30] Numerous organic syntheses[31–34] and some colloidal nanoparticle syntheses[19,21,35] have been optimized using DoE, but all make use of solution-phase methods that can be completed within a few hours. DoE was used to optimize thermoelectric performance in $AgSbTe_2$ by doping, but the general synthetic conditions were unchanged throughout the study.[36] Some phase change studies of shape-memory alloys[22–24] have been performed using DoE, but the phase changes studied therein occur on a timescale much shorter than a traditional week-long solid-state synthesis. To the best of our knowledge, there are no published examples of solvent-free chemical synthesis processes optimized using statistical DoE tools.

Herein, we applied a fast hydride synthesis route to Ni-doped $(Ba/Sr)Fe_4Sb_{12}$ skutterudites. By making use of commercially available software, for the first time, we use a design of experiments tool to optimize solid-state synthesis, yielding single-phase products in a multi-component system. We further evaluated the thermoelectric properties of the synthesized skutterudites in the context of valence electron counting, carrier concentrations, and thermal transport properties influenced by filler identity and framework doping, achieving a peak zT of 0.54 at 673 K for $Sr_{0.92}Fe_{3.28}Ni_{0.70}Sb_{12}$.

Experimental

Synthesis

Warning! Hydrides are air-sensitive and become pyrophoric after ball milling. Use inert atmospheres for handling or transfers of reagents. When heated, hydrides release hydrogen gas. Crucibles used for hydride reactions must allow the diffusion of hydrogen gas or withstand the pressure generated by the reaction. Outer containers must be able to vent overpressure or accommodate evolved gases without bursting.

All weighing of chemicals was performed in an argon-filled glovebox (LC Tech, O_2 < 0.5 ppm) and all ball-mill vials were sealed inside two polyethylene bags to retain the inert atmosphere during mixing or crushing. Barium hydride (BaH_2, 99.7%, Materion), strontium hydride (SrH_2, 99.5%, Materion), iron (Fe, 99.998%, Alfa Aesar), and nickel (Ni, 99.996%, Alfa Aesar) were acquired as powders and used as received. Antimony shot (Sb, 99.9999%, Alfa Aesar) was pulverized to fine powder by two 30 min long rounds of ball-milling in a SPEX 8000M ball mill using a polycarbonate grinding vial with tungsten carbide cap inserts and tungsten carbide balls. Powders of BaH_2 or SrH_2, Fe, Ni, and Sb were loaded into a polycarbonate ball mill vial with a methacrylate or polycarbonate ball at the bottom for mixing in the ball mill. Mixed powders were brought into a glovebox (LC Tech, <1 ppm O_2) equipped with water-cooled TIG welding equipment and transferred into 10 mm diameter by 50 mm long Ta crucibles, which were sealed by arc welding. Once hermetically sealed, crucibles were removed from the glovebox and transferred into a two-part reusable silica reactor. The reactors were evacuated below 30 μbar before loading into the furnace to protect the crucibles inside from oxidation at elevated temperatures. All samples were heated to their target temperatures in 6 hours and annealed for 16 hours. The furnace was switched off, and samples cooled in the furnace with the door closed. Once cool, the crucibles were cut open in the glovebox. Products were usually fine grey powders, although some larger polycrystalline lumps formed sporadically. After grinding gently, samples were stored in the glovebox. Small portions of each sample were removed from the glovebox for characterization.

The duration of ball-milling depended on sample size: 6 minutes for 0.5 gram samples and 18 minutes for the 2.2 gram samples that were used for thermoelectric property measurements. Fe and Ni content was varied around the stoichiometries $Sr_{0.92}Fe_{2.98\pm x}Ni_{1.00\pm x}Sb_{12}$ or $Ba_{0.9}Fe_{3.00\pm x}Ni_{1.00\pm x}Sb_{12}$ where x is 0.15 or 0.30. The total sum of Fe and Ni stoichiometry is 4 in $Ba_{0.9}Fe_{3.00\pm x}Ni_{1.00\pm x}Sb_{12}$, and 3.98 in $Sr_{0.92}Fe_{2.98\pm x}Ni_{1.00\pm x}Sb_{12}$. For Ni-rich Ba-filled skutterudite samples, less BaH_2 was used, their compositions were $Ba_{0.85}Fe_{2.85}Ni_{1.15}Sb_{12}$ and $Ba_{0.85}Fe_{2.70}Ni_{1.30}Sb_{12}$. Ba-containing samples with 3 or more equivalents of Fe were heated to 855 K on the 0.5 g and 2.2 g scale. Samples of the composition $Ba_{0.85}Fe_{2.85}Ni_{1.15}Sb_{12}$ and $Ba_{0.85}Fe_{2.70}Ni_{1.30}Sb_{12}$ and all Sr-containing samples were heated to 893 K.

Characterization

Laboratory powder X-ray diffraction. Powder X-ray diffraction (PXRD) was performed using a Rigaku MiniFlex 600 benchtop diffractometer with a Cu Kα source and Ni Kβ filter. Phase analysis was performed in Match! 3 (Crystal Impact)[37] or PDXL-2 (Rigaku) and Rietveld refinements were performed in GSAS-II.[38] Unit cell parameters of skutterudites were refined using LaB_6 (Alfa Aesar, 99.5% REO) as an internal standard ($a =$ 4.154 Å).

High-temperature synchrotron powder X-ray diffraction. High-temperature *in situ* powder X-ray diffraction (HT-PXRD) data were collected at beamline 17-BM at the Advanced Photon Source, Argonne National Laboratory (APS ANL) on ball-milled BaH_2, Fe, Ni, and Sb precursors mixed in the atomic ratio 0.8 : 3:1 : 12. Precursor powder was loaded into 0.7 mm outer diameter capillaries, which were filled so that the bottom 1 cm contained powder. The capillaries were sealed under vacuum with enough headspace to accommodate released H_2 gas. A typical sealed capillary was 7 cm long. With adequate headspace and the small amount of BaH_2 needed to achieve skutterudite stoichiometry, no capillaries exploded during HT-PXRD data collection. An X-ray wavelength of 0.24079 Å was used. One diffraction pattern was taken per minute during the heating of a sample capillary located between two resistive heater coils. The heating rate of 20 K min^{-1} from room temperature to 1070 K and cooling rate of 20 K min^{-1} from 1070 K to room temperature were utilized. The capillaries were rocked up and down during irradiation to scan more of the sample to counteract the temperature gradient caused by the convection of hot air around the sample. Temperatures were measured by a static thermocouple placed 0.2 mm below the lowermost point reached by the capillary during its vertical travel. The vertical setup was used, similar to the horizontal setup described elsewhere.[39] Phases were identified using Match! 3 (Crystal Impact)[37] or PDXL-2 (Rigaku) and Rietveld refinements were performed in GSAS-II software.[38]

Scanning electron microscopy and energy-dispersive X-ray spectroscopy. Scanning electron microscopy and energy dispersive X-ray spectroscopy (SEM-EDXS) were performed under high vacuum on a JEOL IT200 electron microscope equipped with a backscattered electron detector or an FEI Quanta 250 FEG electron microscope with an Oxford Instruments X-Max EDXS module (80 mm^2 detector). The pellets consolidated by spark plasma sintering were used for SEM-EDXS analysis.

Spark-plasma sintering. Spark plasma sintering (SPS) was performed using a Fuji Industrial Electronics Dr Sinter Lab model 211Lx. Samples used to measure thermoelectric properties were compacted in graphite dies with an inner diameter of 13.1 mm, which were lined with graphite foil to make the inner diameter 12.7 mm. The powder samples (2.1–2.2 grams) were compacted into pellets. Pressure was applied as temperature increased so that the maximum load was applied at the beginning of the temperature dwell. Cooling was uncontrolled in all cases, and pressure was released slowly during the initial rapid cooling. For all samples, approximately 80 MPa remained while cooling through 523 K, and the rest was released so that displacement of the upper electrode did not observably change until 400 K. Remaining pressure was released by 350 K, and cooling to room temperature occurred under a static pressure of approximately 5 MPa. Geometric densities of sintered pellets were calculated from linear dimensions and masses of pellets, assuming cylindrical geometry. Archimedean densities were calculated using Archimedes' method from the weights of the pellet in air and toluene ($\rho = 0.867$ g ml^{-1}). Pellet compactness is summarized in Table S1.†

Samples of $Ba_{0.9}Fe_{3.00\pm x}Ni_{1.00\pm x}Sb_{12}$ with 3 or more equivalents of Fe were sintered by heating to 773 K over 10 minutes, followed by 10 minutes of dwell time at 773 K using 90 ± 2 MPa of pressure. Samples of $Ba_{0.9}Fe_{3.00\pm x}Ni_{1.00\pm x}Sb_{12}$ with less than 3 equivalents of Fe were sintered by heating to 873 K in 11 minutes with a 10 minute dwell under 100 ± 2 MPa of pressure to remove a small impurity of $BaSb_3$, discussed further in the ESI.† Sr-containing samples with 2.68–3.28 equivalents of Fe were sintered by heating to 773 K in 10 minutes and dwelling at 773 K for 10 minutes. 90 ± 2 MPa of pressure were used for the other pellets except $Sr_{0.92}Fe_{2.83}Ni_{1.15}Sb_{12}$, which was compressed with 100 ± 2 MPa of pressure. $Sr_{0.95}Fe_{3.43}Ni_{0.55}Sb_{12}$ was sintered by heating to 673 K in 10 minutes, followed by a 10 minute dwell at 673 K and 168 MPa, the maximum pressure possible for a 12.7 mm pellet in the available tooling.

High-temperature thermoelectric properties. Prior to the measurement of transport properties above room temperature, the thermal stability of each pellet was confirmed by PXRD and by evaluating pellet mass change after heating to 773 K in 45 minutes and dwelling for one hour under industrial-grade argon flow in a tube furnace. Seebeck coefficients and electrical conductivities were measured on uncoated SPS densified pellets under flowing ultra-high purity argon in a Netzsch Nemesis 458 SBA in the temperature range of 298 K to 673 K. Pellets were coated with graphite using an aerosol spray for thermal diffusivity measurements in a Netzsch Hyperflash 457 HT LFA under flowing ultra-high purity argon. A pyroceram standard (Netzsch) was used for temperature-dependent thermal diffusivities and specific heats. Reported thermal conductivities in the range of 298–673 K were calculated from the measured thermal diffusivity: $\kappa = \alpha C_p d$, where α is the measured thermal diffusivity, C_p is the specific heat capacity estimated using the Dulong–Petit law, and d is the measured density of the pellet. Specific heat capacity was calculated using the geometric or Archimedean density, whichever was closer to 95%.

Hall effect measurements. After high-temperature thermoelectric measurements were completed, the pellets were cut into 6 mm by 9 mm rectangular bars using a low-speed diamond saw. The cutting oil was washed off with multiple rinses of hexanes, and the graphite coatings were then removed by polishing with 2500 grit sandpaper. Hall measurements were performed at 200 K, 250 K, and 300 K using a Quantum Design physical properties measurement system (PPMS) with the electrical transport (ETO) module under magnetic fields ranging from 3 T to −3 T by increments of 0.5 T.

Statistical analysis and design of experiments. The JMP Pro 16 software package (Statistical Discovery LLC) was used for the statistical analysis of selected synthesis data for $BaFe_3NiSb_{12}$, while statistical design of experiments (DoE) was used to find the optimal loading composition and reaction temperature for synthesis of phase-pure $SrFe_3NiSb_{12}$. In both cases, the model was built using the "Custom Design" tool in JMP, which uses Mayer and Nachtsheim's coordinate-exchange algorithm.[40,41]

Experimental data produced during the optimization process for $BaFe_3NiSb_{12}$ was input into a response-surface model (RSM) with parallel screening of variables. To use DoE methodology for statistical analysis within JMP, the "custom design" tool was used with uncontrolled variables. The loading stoichiometries of all precursors and dwell temperatures were inherently constrained to experimentally attempted values, defined in Table 1. In addition to these factors, statistical analysis used the quadratic interaction terms Ba stoich. × temp., Ba stoich. × Fe stoich., Ba stoich. × Ni Stoich., Fe stoich. × Ni stoich., Fe stoich. × temp., and Ni stoich. × temp. Antimony loading stoichiometry was set at 12 to normalize the stoichiometry of the other reagents and was not optimized in the statistical model. "Purity" was the phase fraction of skutterudite determined by full-profile fitting using Match! 3 software.[37] To ensure accuracy, phase fractions (wt%) were also determined by Rietveld refinement using GSAS-II software[38] and found to be consistent (±2–3 wt%) with those determined using Match! 3. Over 100 000 random starts were used to optimize the model.

Table 1 Summary of factors with the respective constraints used for statistical analysis of $BaFe_3NiSb_{12}$ synthesis to maximize the fraction of skutterudite phase (response)

$Ba_aFe_bNi_cSb_{12}$	
Factors	Ranges
Ba stoichiometry, a	$0.71 \le Ba \le 1.22$
Fe stoichiometry, b	$2.71 \le Fe \le 3.03$
Ni stoichiometry, c	$0.95 \le Ni \le 1.31$
Dwell temperature, T (K)	$773K \le T \le 973$ K
Response: purity	Maximized within the range 0–100%

Table 2 Summary of factors and constraints used for the design of experiments to maximize the fraction of $SrFe_3NiSb_{12}$ skutterudite (response)

	$Sr_aFe_bNi_cSb_{12}$
Factors	Ranges
Sr stoichiometry, a	$0.7 \le SrH_2 \le 1.1$
Fe stoichiometry, b	$2.7 \le Fe \le 3.3$
Ni stoichiometry, c	$0.7 \le Ni \le 1.3$
Dwell temperature, T (K)	$873K \le T \le 933$ K
Fe + Ni (constraint)	$3.97 \le b + c \le 4.0$
Response: purity	Maximized within the range 0–100%

The synthetic optimization of $SrFe_3NiSb_{12}$ was performed using the JMP software package to generate a response surface model (RSM) with parallel screening of variables. One center point was used. Constraints were implemented based on preliminary reactions. Table 2 lists the allowed ranges for each factor. In addition to these factors, DoE used the quadratic interaction terms: Sr stoich. × temp., Sr stoich. × Fe stoich., Sr stoich. × Ni Stoich., Fe stoich. × Ni stoich., Fe stoich. × temp., and Ni stoich. × temp. Prior experience dictated that a slight excess of Sb may be needed to account for side-reactions with the crucible walls. Therefore, loading stoichiometries of Fe and Ni were constrained so that total transition metal stoichiometry remained between 3.97 and 4.0 molar equivalents, normalized to 12 molar equivalents of Sb. Relative phase fractions (wt%) were estimated *via* full-profile fitting using Match! 3 software.[37] 2224 random starts were used to optimize the model.

Results and discussion

Hydride synthesis route for skutterudites

Preparation of Sr and Ba-filled skutterudites using SrH_2 or BaH_2 as precursors for the filler atoms confers significant advantages over synthesis using Sr or Ba metals (Fig. 1). Hydrides of alkaline earth metals are readily available as fine powders and, therefore, can be mixed with the rest of the powder precursors in a low-energy ball mill, resulting in a homogenous reaction mixture. Intimate mixing and the increased reactivity of alkaline earth hydrides over alkaline earth metals both contribute to decreasing the temperature and duration of a chemical reaction.[42] The advantages of hydride synthesis have been previously demonstrated by examples of new and known compounds in alkali metal (Na, K) – d block metal (V, Zn, Cd) – Sb phase spaces.[42–48] Using BaH_2 instead of Ba metal when preparing K- or Co-doped $BaFe_2As_2$ superconductors allowed the reduction of synthesis temperatures and annealing durations.[47,48] For the synthesis of antimonides, typical hydride route reaction profiles are a day long and require heating below 900 K.[42–46] The synthesis conditions herein (Fig. 1) contrast with typical syntheses reported in the literature for Ni-containing skutterudites, which require two separate annealing steps at higher temperatures. The first heating usually occurs at a temperature between 1350 K and 1523 K, then quenching in air or water, and the second annealing extends for 2–7 days.[13–15,25–30,49]

High-temperature *in situ* powder X-ray diffraction

Due to intimate precursor mixing, reactions involving hydride precursors occur within minutes, enabling their progression to be monitored in real-time, thus allowing one to peer into the "black box" of solid-state synthesis using synchrotron high-temperature *in situ* powder X-ray diffraction (HT-PXRD). This makes it possible to find optimal synthesis temperatures with a single experiment, and gain insight into what intermediates lead to the formation of the desired phase – the closest a solid-state chemist can get to organic chemistry-like understanding of their reaction mechanisms. It is important to note here that a solid solution exists between marcasite-type $FeSb_2$ and marcasite-type $NiSb_2$ (space group *Pnnm*, #58).[50] Increasing Ni-content in the marcasite solid solution $Fe_{1-x}Ni_xSb_2$ causes extension of the c-parameter and contraction of the a-parameter. As a result, the position and splitting of two sets of doublet peaks corresponding to Miller indices (*hkl*) of (111), (210) and (121), (220)[51] at Q values of approximately 2.2 $Å^{-1}$ show changes as Fe and Ni are exchanged for one another. Therefore, these peaks can be used to estimate the Fe to Ni ratio in $Fe_{1-x}Ni_xSb_2$ marcasites, which was important to studying the mechanism of skutterudite formation.

The HT-PXRD data used to study the reaction between BaH_2, Fe, Ni, and Sb is shown in Fig. 2. Upon initial heating, all Bragg peaks shift progressively to lower Q values, indicating expansion of the unit cells of unreacted precursors with increasing temperature. $BaSb_3$ and marcasite-type $FeSb_2$ form at 616 K (Fig. S1†). A skutterudite phase begins to form at 755 K together with small amounts of marcasite-type $NiSb_2$ (Fig. S2†). Once the temperature exceeds 835 K, Bragg peaks for all the binaries except $NiSb_2$ disappear. At 855 K, the skutterudite phase is the major crystalline phase with only a trace amount of $Fe_{0.75}Ni_{0.25}Sb_2$ present (Fig. S2†). The skutterudite decomposes into $Fe_{0.75}Ni_{0.25}Sb_2$ and NiSb at 916 K (Fig. S2†). Above 936 K, only the broad, elevated background of the melt and NiSb Bragg peaks match known phases until cooling through 890 K (Fig. S3†). Ni_5Sb_2 and marcasite-type $Fe_{0.75}Ni_{0.25}Sb_2$ crystallize when cooled below 890 K, with some Sb and the extant NiSb. A skutterudite phase, $Ba_{1.5}Sb_3$, Sb, and marcasite-type $Fe_{0.75}Ni_{0.25}Sb_2$ are observed at 850 K and below as cooling continues (Fig. S3†). No changes in phase or further chemical reactions are visible during cooling below 850 K.

From the *in situ* data, we can conclude that the filled skutterudite phase $BaFe_3NiSb_{12}$ forms from a mixture of unreacted Sb with $BaSb_3$, $FeSb_2$, and $NiSb_2$ binary intermediates produced during heating. This reaction pathway offers an important hint as to why the exact Fe/Ni ratio is not very important to the purity of the final skutterudite phase, enabling the synthesis of $BaFe_{3.30}Ni_{0.70}Sb_{12}$ at the same temperature as $BaFe_3NiSb_{12}$. Based on *in situ* diffraction data, $FeSb_2$ and $NiSb_2$ act as the primary Fe and Ni sources for skutterudite formation. Phase

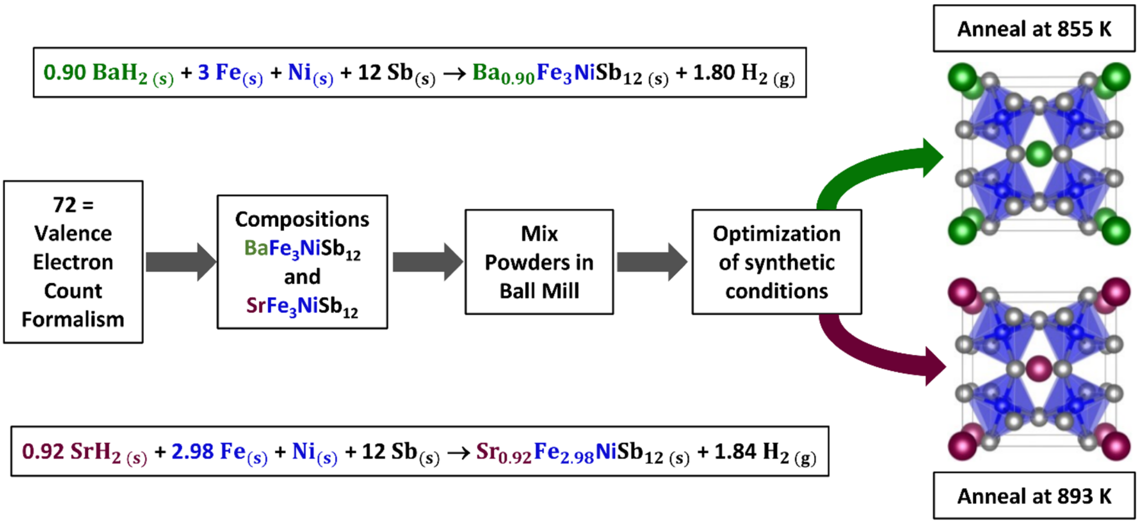

Fig. 1 Overview of the preparation of skutterudites as performed herein. Samples were heated to their annealing temperature within 6 hours and annealed for 16 hours.

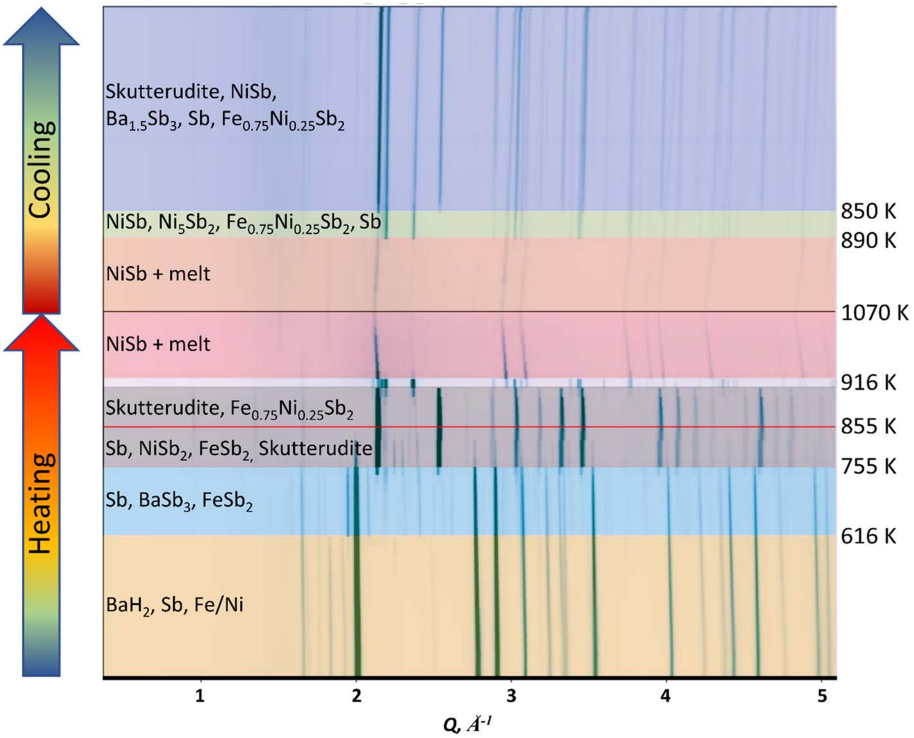

Fig. 2 High-temperature *in situ* powder X-ray diffraction data obtained upon heating to 1070 K and subsequent cooling of a BaH_2, Sb, Fe, Ni precursors mixture. Data represented as a contour plot, and each horizontal section corresponds to a PXRD pattern where darker shading indicates higher relative diffraction intensity. The temperature ranges with distinct crystalline phases present are highlighted in yellow, light blue, grey, pink, orange, light green, and blue.

analysis of *ex situ* powder X-ray diffraction data from synthesis attempts at various temperatures and Ba stoichiometries offers further insight into the reaction mechanism and reproducibility of 2.2 g-scale reactions when making $Ba_{0.9}Fe_{3.00\pm x}Ni_{1.00\pm x}Sb_{12}$.

Reactions in the laboratory occur under different conditions than *in situ* reactions. However, the same intermediates and decomposition products are shown in the *ex situ* PXRD patterns, such as the $BaSb_3$ resulting from a small excess of BaH_2 in Fig. 3A. *Ex situ* reactions above the optimal temperature produce NiSb and $Fe_{0.75}Ni_{0.25}Sb_2$ impurities due to decomposition of the skutterudite, as in Fig. 3B. NiSb is seen throughout the HT-PXRD data as a decomposition product. In *ex situ* diffractograms, NiSb is also seen in samples that were not heated to a high enough temperature. NiSb is quite thermally stable, so it is likely the last binary to react and the first decomposition product to form. Therefore, the presence of NiSb alone in a sample is not diagnostic of synthesis temperatures being too low or too high. When NiSb is accompanied by $BaSb_3$ and binary marcasites $FeSb_2$ and $NiSb_2$, the combination of impurities indicate that synthesis temperatures were too low, as these binaries would further react to form a skutterudite phase at higher temperatures. Samples with NiSb and $Fe_{0.75}Ni_{0.25}Sb_2$ together indicate that the annealing temperature was too high, leading to skutterudite decomposition.

Increased Ni content in the samples with loading compositions $Ba_{0.90}Fe_{2.70}Ni_{1.30}Sb_{12}$ and $Ba_{0.90}Fe_{2.85}Ni_{1.15}Sb_{12}$ resulted in an increased phase fraction of NiSb, necessitating the increase in optimal annealing temperature from 855 K (Fig. 3A) to 893 K (Fig. 3C) in 2 gram reactions. Excessive BaH_2 content results in a $BaSb_3$ impurity, which has visible Braggs' peaks in the Ba-rich samples (Fig. 4A, C and G). Temperatures below 855 K result in binary and transition metal-antimony compounds, most of which are marcasite-type $FeSb_2$ and $NiSb_2$. The reaction is temperature-dependent enough that samples annealed within less than 50 K are distinguishable by PXRD. Samples of identical composition annealed at 773 K (Fig. 4F and L) and 823 K (Fig. 4E and K) have different impurities than samples annealed at 873 K (Fig. 4D and J).

Statistical analysis of $BaFe_3NiSb_{12}$ synthesis

The mechanistic understanding afforded by *in situ* studies is a powerful tool for the characterization and optimization of synthesis processes, but few facilities are capable of these experiments. The method traditionally used by solid-state chemists to optimize synthesis relies on the Edison-style approach of changing one variable at a time based on intuition derived from past synthesis experience. While this method is easily applied to simple solid-state systems, multi-parameter optimization, such as the quaternary skutterudites herein, can quickly become cumbersome. The number of variables involved makes it challenging to notice trends without collecting prohibitive amounts of data. Statistical analysis software offers a way to compare the results of experiments in easily understood visual formats or even plan a series of reactions to

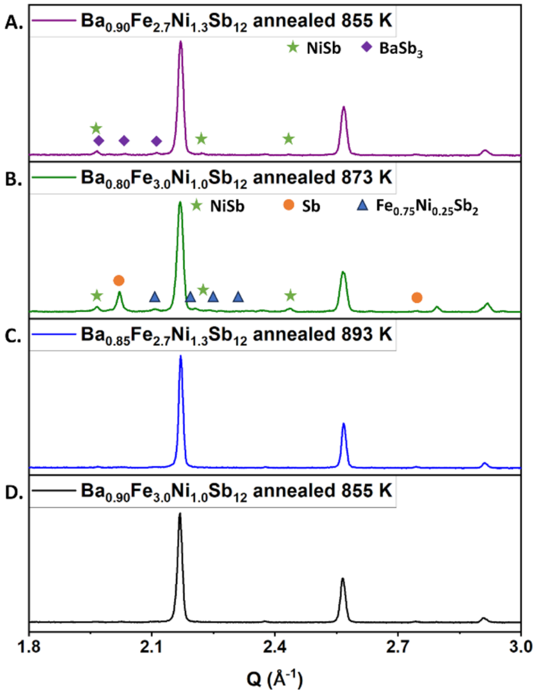

Fig. 3 PXRD patterns collected at room temperature for samples with variation in Ba : Fe : Ni stoichiometry and annealing temperature. Different impurity phases form depending on whether annealing temperature is too high or too low compared to the optimal temperature. Higher Ni content requires a higher annealing temperature, increasing the synthesis temperature from 855 K ($Ni_{1.0}$) to 893 K ($Ni_{1.3}$). (A) Ni-rich sample annealed at too low a temperature. (B) Sample with 3 : 1 Fe : Ni stoichiometry annealed at too high a temperature. (C) Ni-rich sample annealed at the optimal temperature. (D) Sample with 3 : 1 Fe : Ni stoichiometry annealed at the optimal temperature.

minimize the number of trials needed for optimization by taking advantage of the design of experiments (DoE) methodology. However, it is important to note that fully optimizing the synthesis of a compound using DoE tools may take dozens of reactions, making DoE methods unsuitable for longer reactions.

This is most likely why examples of DoE tools applied to inorganic solid-state materials are rare and tend to involve somewhat fast solution-phase syntheses,[21,35] phase transitions,[24] properties optimization,[36] or device fabrication.[52] After all, performing approximately 20–30 experiments to reach one definitive answer makes DoE unappealing when traditional solid-state reactions often take a week or longer.[25–30] The sluggishness of many solid-state reactions is caused by the slow diffusion of solids. Fortunately, solid-state syntheses using hydride precursors are highly reproducible and reasonably fast, with typical durations of approximately 24 hours and no need to regrind and reheat samples.[42] Therefore, quick reactions enabled by hydride precursors make the requisite number of reactions for statistical DoE much less daunting.

A pace of two days to complete three reactions simultaneously makes it possible to gather enough data in a short time to use DoE when performing solid-state synthesis using hydride precursors. To validate the utility of DoE for solid state synthesis, we used previously collected synthesis data and modeled it using uncontrolled continuous variables within the ranges listed in Table 1. Because this is an analysis of existing data and not new experiments, this constitutes a statistical analysis rather than a DoE. Had the data been collected at pre-planned, statistically optimal data points, this would be DoE. A response surface model (RSM) is an n^{th} dimensional surface that relates the values of independent variables, called factors, to the value(s) of the dependent variables, called responses, where n is the "level" (quadratic functions are 2-level, cubic functions are 3-level, *etc.*..) of the model. A 2-level response surface model based on Mayer and Nachtsheim's coordinate-exchange algorithm[40] was used herein. The coordinate-exchange algorithm uses iterative "random starts" to optimize a model. To do this, randomly chosen values of the constants associated with each term in the equation that defines the response surface are replaced with values at the extrema of the surface, and the version of the equation with the lower variance is kept. The global optimum is the equation with the lowest variance. In non-trivial cases, at least 1000 random starts are needed, with greater numbers of starts increasing the chances of finding the globally optimal model.[40,41] There are other model types that are more predictive than RSMs or that require fewer data points, but they would require more data or generate less predictive results, respectively. The software used here, JMP Pro 16 (Statistical Discovery LLC), automatically performs screening of variables (analyzes the importance of all variables to each outcome), highlighting which factors are most important to achieving a desired result. This screening is especially useful for subsequent rounds of optimization[19] because further iterations of a model can be made without unimportant factors, and models with fewer variables require fewer experiments.

Sampling as many different regions of the modeled synthetic space as possible was especially important to the validation of JMP using data shown in Fig. 4 and S4.† These data were collected during attempts to optimize the bulk synthesis of $BaFe_3NiSb_{12}$ before *in situ* data was collected. The model based on these data (Fig. 5) covers the range of temperatures and compositions listed in Table 1 and shown in the loading ratios and annealing temperatures illustrated in Fig. 4 and S4.† The *in situ* PXRD data herein reveal the reaction onset temperature and demonstrate that reactions proceed to near completion within seconds. Based on our prior experience with hydride reactions of pnictides, reactions achieve thermal equilibrium within a few hours of reaching a given temperature, and a fixed heating rate can be used.[42–48] As such, a 16-hour annealing time was deemed to be sufficient to ensure complete reaction and was kept constant across all synthesis attempts.

Limited to the results from previous experimental attempts, every available piece of data had to be used. The PXRD patterns of each product are shown in Fig. 4 and S4.† Fig. 5 and Table 3 show the results of this statistical analysis model. The "desirability" of a factor represents what values that factor can take to achieve an optimal result. If all factors have a desirability of 1, the optimal result should occur.[53] The "LogWorth" is the negative $\log_{10}$ of the p-value.[54] As the p-values decrease,

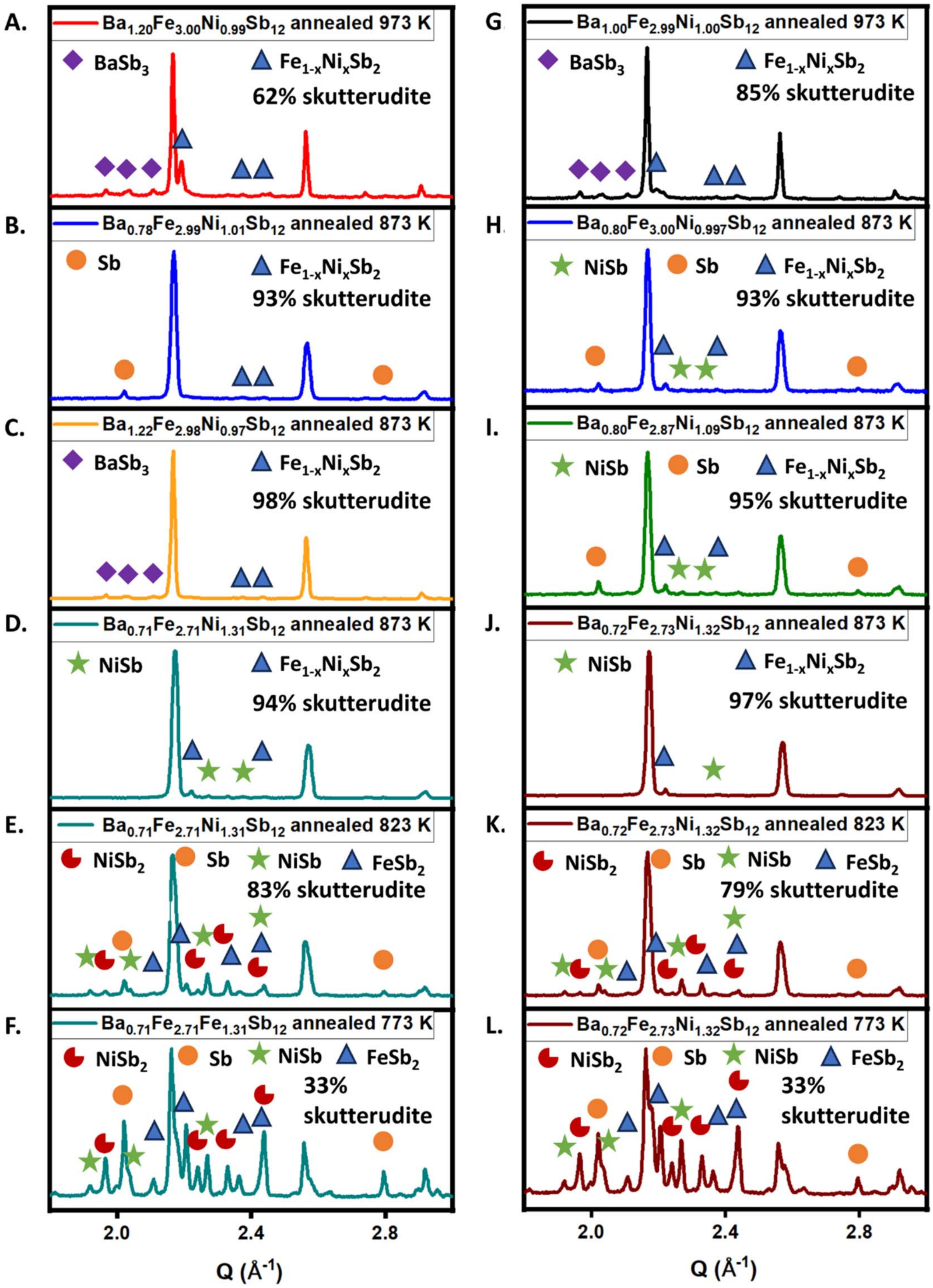

Fig. 4 Abridged powder X-ray diffraction patterns with non-skutterudite peaks denoted using symbols. Each sample (A–L) is identified by its reaction stoichiometry and annealing temperature. The wt% of skutterudite phase was estimated using full-profile fitting. This is the experimental data used to validate the response surface modeling functionality of JMP Pro 16 for the optimization of synthetic conditions to form $BaFe_3NiSb_{12}$.

LogWorth increases, and the more important that factor is to the outcome of an experiment[54] (see ref. 53 for an in-depth discussion of the *p*-value). If LogWorth is above 2, as indicated by the blue vertical lines in Table 3, changes to the factor in question have a statistically significant impact on the response. If LogWorth is under 2, the factor might not be changing the response. If no factor has a LogWorth above 2, something needs troubleshooting: perhaps the model is ill-

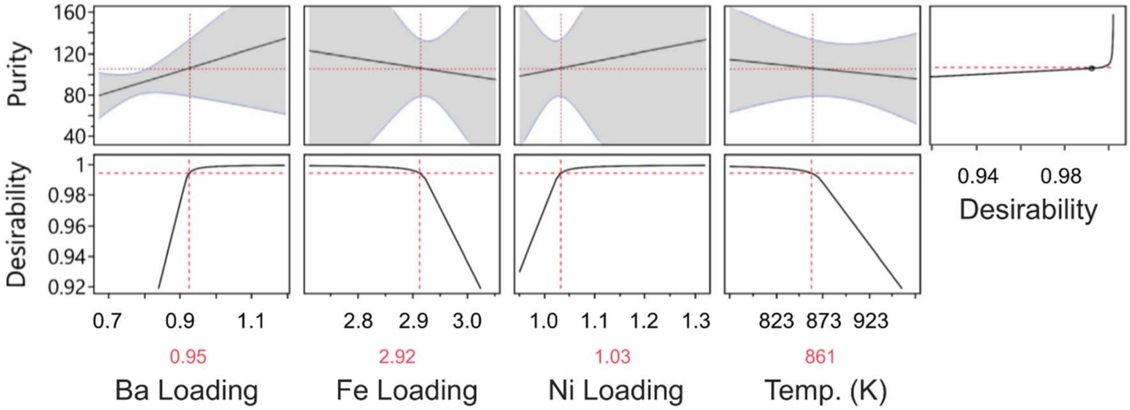

Fig. 5 Output from the statistical analysis of synthesis conditions for $BaFe_3NiSb_{12}$. Large confidence intervals (grey surfaces) in the purity *vs.* factor plots are the result of the biased dataset used for this statistical analysis. Horizontal asymptotes in the desirability *vs.* factor plots indicate that the global optimum may not be within the modeled space, and so the result is limited to estimates of local minima, represented by the sloping line leading to or away from the horizontal asymptote.

Table 3 Results of statistical analysis of $BaFe_3NiSb_{12}$ synthesis optimization. The results are found to be statistically insignificant, as no parameter reaches a LogWorth = 2 (indicated by the blue lines) or more. The factors themselves (in bold) are less significant than 2nd order terms they contribute to

Parameters	LogWorth	PValue
Ba Stoich. * Temp	0.602	0.25026
Fe Stoich. * Ni Stoich.	0.551	0.28101
Ni Stoich. * Temp	0.358	0.43856
Ba Stoich. (0.7,1.22)	0.323	0.47526
Temp, K (773,973)	0.212	0.61310
Fe Stoich. (2.71,3.05)	0.158	0.69469
Ba Stoich. * Fe Stoich.	0.134	0.73516
Ni Stoich. (0.95,1.32)	0.131	0.73974
Fe Stoich. * Temp	0.121	0.75662
Ba Stoich. * Ni Stoich.	0.092	0.80994

defined, the dataset is biased or too small, or the process undergoing optimization is irreproducible. In our case, the dataset is biased. The data significantly oversamples stoichiometry of approximately $Ba_{0.8}Fe_{3.0}Ni_{1.0}Sb_{12}$ with annealing at 873 K. Grey surfaces in Fig. 5 are the confidence intervals for each factor. The further the grey area extends from the black line inside it, the larger the confidence interval, and the less precise (and potentially less accurate) the model is. The pinched shapes of grey surfaces (Fig. 5) in the purity *vs.* factor plots and the high importance of the Fe stoich. × Ni stoich. quadratic term (Table 3) primarily indicate the biases in the data. Fe and Ni were exchanged for one another during synthesis because the target was a solid solution of skutterudites $Ba_{0.9}Fe_{3.00\pm x}Ni_{1.00\pm x}Sb_{12}$, therefore, the sum of Fe and Ni stoichiometry must be 4, the required stoichiometry to form skutterudites.

The importance of Fe and Ni stoichiometry was exaggerated relative to temperature and Ba stoichiometry because of the exchange of Fe and Ni to maintain a total stoichiometry of 4. The ratio between Fe and Ni is known not to matter because any Fe/Ni can be used within the defined limits when performing reactions on a half-gram scale. Fe–Ni stoichiometric variations had to be modeled because the only samples annealed under 873 K had varying Fe and Ni stoichiometries. Therefore, the possibility of Fe and Ni stoichiometry having a meaningful effect on synthesis temperature could not be ignored. On the half-gram scale, no difference in optimal annealing temperature was noted across the $Ba_{0.9}Fe_{3.00\pm x}Ni_{1.00\pm x}Sb_{12}$ compositions. All data used to make the model was taken from 0.5 g scale reactions. Therefore, the model had no way to account for the need to use less BaH_2 and anneal Ni-rich $Ba_{0.9}Fe_{3.00\pm x}Ni_{1.00\pm x}Sb_{12}$ samples at a higher temperature than Fe-rich samples in reactions performed on the 2.2 gram scale (see Experimental for synthesis details). The synthetic conditions recommended by the model were a sample with loading composition 0.95 BaH_2 + 2.92 Fe + 1.03 Ni + 12 Sb annealed at 861 K. This is remarkably close to the optimal compositions used to make samples, especially the most important – temperature. The accuracy of this model in predicting successful synthesis conditions highlights the importance of preliminary reactions and well-chosen ranges for each parameter when setting the limits of a model. The center of the modeled space (average of the high and low limits) should be near the expected optimal value so that the software can calculate meaningful regression statistics on all sides of the global minimum in the difference between the regression (model) and experimental data. Furthermore, no result can be recommended outside the space in which the model is defined. Therefore, one must encompass the optimal reaction conditions within the modeled space without making the range of possible conditions so large that meaningful results can hide in the empty space between data points.

The loading stoichiometry ($Ba_{0.90}Fe_{3.00}Ni_{1.00}Sb_{12}$) was chosen based on the VEC formalism and trial-and-error. Annealing at 855 K was chosen based on HT-PXRD experiments. $Ba_{0.90}Fe_{3.00}Ni_{1.00}Sb_{12}$ samples annealed at 855 K result in samples composed of the desired skutterudite phase and a miniscule amount of unreacted Sb. Given a small and imperfect dataset, the model's ability to come within a margin of 6 K from an experimentally measured optimal temperature is very impressive (861 K *vs.* 855 K) within the total range of 200 K. Therefore, the authors contend that the model is successful despite sampling biases in the experimental data points selected for the model (Fig. 4 and 5). These biases (and lack of constraints) caused the deviation from optimal stoichiometry. In short, the data set chosen for this model oversampled annealing at 873 K. There were no samples annealed below 873 K with Fe stoichiometry significantly different from 2.7 and Ni stoichiometry differing from 0.7. As a result, the model cannot fully deconvolute the importance of temperature from the importance of Ni stoichiometry. However, this sampling bias would not hinder carefully designed optimization processes that use DoE from the beginning.

Design of experiments for $SrFe_3NiSb_{12}$ synthesis

Based on prior experience with the $BaFe_3NiSb_{12}$ synthesis model and the assumption that the same formation mechanism applies to $SrFe_3NiSb_{12}$, we attempted a DoE-based optimization of $SrFe_3NiSb_{12}$ synthesis using the coordinate-exchange algorithm. Laboratory PXRD data indicated that an annealing temperature of 873 K is close to the optimal temperature, since reaction products were primarily skutterudite with small phase fractions of binary impurities and unreacted antimony (Fig. S5†). The annealing temperature of 973 K was found to be too high because samples contained $Fe_{1-x}Ni_xSb_2$ marcasite-type impurities. Because 873 K was tantalizingly close to the optimal temperature, and 973 K was known to be too far, the temperature limits for the DoE optimization (Fig. S5 and S6†) were chosen as 873 K and 933 K. By using a smaller range of temperatures and SrH_2 stoichiometry (Table 2), any effects of Fe and Ni stoichiometry could be studied in more detail.

By analogy to $Ba_{0.9}Fe_{3.00\pm x}Ni_{1.00\pm x}Sb_{12}$, we postulate that exact Fe and Ni stoichiometry should not matter if the sum of Fe and Ni stoichiometries remains between 4 and 3.97. However, Fe and Ni stoichiometries were modeled in case $Sr_{0.92}Fe_{2.98\pm x}Ni_{1.00\pm x}Sb_{12}$ was less analogous to $Ba_{0.9}Fe_{3.00\pm x}Ni_{1.00\pm x}Sb_{12}$. The sum of Fe and Ni stoichiometries was confined to the range $3.97 \leq \text{total} \leq 4.0$ in the case of DoE optimization of $Sr_{0.92}Fe_{2.98\pm x}Ni_{1.00\pm x}Sb_{12}$ synthesis. Sr stoichiometry was modeled in the range from 0.7 to 1.1 equivalents, with the lower boundary corresponding to the minimal probable filling fraction of Sr into the central voids of the skutterudite structure as estimated by SEM/EDXS, while the upper boundary was selected based on the maximum equivalents of SrH_2 that do not result in excessive phase fractions $SrSb_2$ impurity detectable by laboratory PXRD. Modeling the strontium stoichiometry is important because insufficient filler metal will

Table 4 Results of DoE optimization of $SrFe_3NiSb_{12}$ synthesis. The results are found to be statistically insignificant, as no parameter reaches a LogWorth = 2 (indicated by the blue lines) or more. The factors themselves (in bold) are less significant than 2nd order terms they contribute to

Source	LogWorth	PValue
Sr Stoich.*Temp.	0.557	0.27703
Sr Stoich.(0.7,1.1)	0.512	0.30760
Fe Stoich.*Sr Stoich.	0.511	0.30808
Ni Stoich.*Sr Stoich.	0.499	0.31691
Ni Stoich.*Temp.	0.295	0.50675
Fe Stoich.*Temp.	0.272	0.53515
Ni Stoich.(0.7,1.3)	0.206	0.62272
Temp.(873,933)	0.193	0.64146
Fe Stoich.(2.67,3.3)	0.162	0.68897
Temp.*Temp.	0.117	0.76438
Ni Stoich.*Ni Stoich.	0.043	0.90640
Fe Stoich.*Ni Stoich.	0.036	0.92142
Sr Stoich.*Sr Stoich.	0.029	0.93557
Fe Stoich.*Fe Stoich.	0.029	0.93640

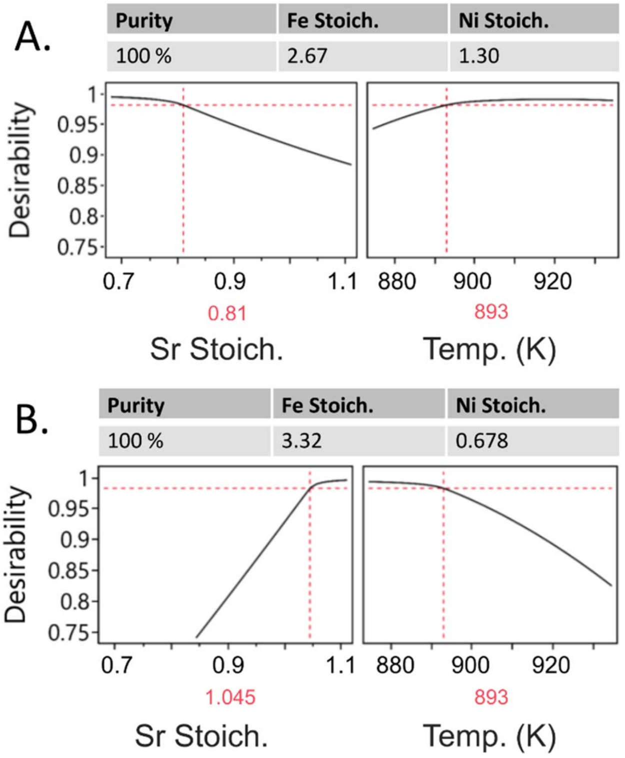

Fig. 6 The optimal synthesis conditions for the end members of the solid solution $Sr_{0.92}Fe_{2.98\pm x}Ni_{1.00\pm x}Sb_{12}$ according to DoE. (A) Sr stoichiometry *vs.* desirability and temperature *vs.* desirability, with the optimal Sr loading predicted to be 0.81 equivalents at the minimum optimal temperature of 893 K. (B) Sr stoichiometry *vs.* desirability and temperature *vs.* desirability, with the optimal Sr loading predicted to be 1.045 equivalents at the maximum optimal temperature of 893 K.

result in deviations from the nominal valence electron count and decrease the number of rattler atoms available to dissipate phonons. Excess Sr causes the formation of Sr–Sb air-sensitive binary impurities that could alter the properties of a pellet. The "boxes" defined by factors (Tables 2 and 4) that encompass the phase space within the RSM model are illustrated in Fig. 6. The model was designed with a center point (experiments at the exact center of the modeled "box") to examine the reproducibility of the process, and 15 screening points (experiments at varying conditions) were used to find an experimental "best guess" as to what optimal synthesis conditions should be. We did not use replicate trials because we decided that conserving materials and getting results quickly was more important than assuring the statistical significance of our results, especially considering the accuracy of the model of the Ba-filled skutterudites considered earlier.

The suggested optimal conditions (red lines in Fig. 6A and B) indicate that 0.81 to 1.05 equivalents of SrH_2 should be optimal, depending on Ni stoichiometry, and an annealing temperature of 893 K is preferred at all compositions. Only 2224 random starts of the coordinate exchange algorithm were used to optimize four continuous variables with one response, which is rather few,[40,41] and the results were statistically insignificant. Nevertheless, the generated model remains very useful. The most important terms were Sr stoichiometry and the quadratic term relating Sr stoichiometry and annealing temperature (Table 4). The next most important terms are the Sr stoichiometry itself and the quadratic terms that involve Sr stoichiometry. This is expected based on the analogy to the statistical analysis of $Ba_{0.9}Fe_{3.00\pm x}Ni_{1.00\pm x}Sb_{12}$ synthesis.

Technically, the results of DoE optimization were statistically insignificant, as LogWorth was below 2 for all parameters (left of the blue line in Table 4). Hence, optima were predicted to exist at the extrema of Fe and Ni stoichiometry. However, careful analysis of the model and PXRD data (Fig. S5 and S6†) allows one to extract useful information from this round of DoE. $Sr_{0.92}Fe_{2.98\pm x}Ni_{1.00\pm x}Sb_{12}$ is part of a solid solution where x is small, so Vegard's rules should apply. Following Vegard's rules, if 893 K is the optimal annealing temperature for Fe-poor ($Fe_{2.67}Ni_{1.30}$) and Fe-rich ($Fe_{3.32}Ni_{0.678}$) compositions, 893 K should also be optimal for the stoichiometries between the extrema. By examining the secondary phases in our reaction products, we can validate the predicted optimal temperature. Ternary marcasite $Fe_{1-x}Ni_xSb_2$ forms when annealing at 903 K and 933 K, and binary marcasites $NiSb_2$/$FeSb_2$ form at 873 K (Fig. S5 and S6†). Binary marcasites are precursors to skutterudite, while ternary marcasite is a decomposition product. Therefore, the optimal temperature for skutterudite synthesis must be between 873 K and 903 K, so the temperature of 893 K predicted by DoE is a reasonable result. Therefore, with the right amount of SrH_2, the annealing temperature should be set to 893 K for any Fe/Ni ratio. The DoE model suggests that the Fe-rich ($Fe_{3.32}Ni_{0.678}$) composition requires 1.05 equivalents of SrH_2, and the Fe-poor composition ($Fe_{2.67}Ni_{1.30}$) needs only 0.81 equivalents of SrH_2 (Fig. 6). Following Vegard's rules, a sample with the composition $Sr_{0.92}Fe_{2.98}Ni_{1.00}Sb_{12}$ annealed at 893 K should be pure. Exactly such a sample showed no binary or ternary impurities on the 2 gram scale (Fig. S7†). Ultimately, regardless of Fe and Ni stoichiometry, 0.92 equivalents of SrH_2 provided pure $Sr_{0.92}Fe_{2.98\pm x}Ni_{1.00\pm x}Sb_{12}$ samples with $x \leq 0.3$. On the 0.5 g scale, laboratory PXRD experiments showed the products contained minor impurities of Sb, $FeSb_2$, and $NiSb_2$ in addition to skutterudite (Fig. S7†). Further reactions revealed that this scale dependence is merely a case of transfer losses affecting the least plentiful reagent disproportionately, discussed further in the ESI (Fig. S7†). Because 2 gram samples are required to press pellets for high-temperature thermoelectric property measurements, synthesis at the 0.5 gram scale was not pursued further.

General guide to statistical DoE, using hydride synthesis of skutterudites as an example

How many preliminary reactions would have to be run to find usable boundaries for the RSM without prior knowledge of hydride precursor reactions or previous experience making alkaline earth-filled FeNi skutterudites? A brief literature survey reveals that skutterudites are usually made from reaction mixtures that are stoichiometric or nearly stoichiometric, so 1-4-12 stoichiometry should be good enough for preliminary reactions. Hydride reactions tend to take place within 16 to 36-hour-long heating profiles, so it's worth trying one short-, medium-, and long-duration preliminary reaction. Synthesis *via* the hydride route is also performed as a one-step annealing at temperatures that are hundreds of Kelvin lower[42–48] than a typical solid-state reaction. If solid-state synthesis of a skutterudite is typically performed between 1523 K and 1350 K, surveying temperatures at 100 K increments from 1300 K down to 800 K results in six trials to get a rough temperature range. These result in nine preliminary reactions to find an appropriate range of dwelling times and temperatures. If desired, these preliminary reactions can be retroactively analyzed using statistical methods, like the example of $Ba_{0.9}Fe_{3.00\pm x}Ni_{1.00\pm x}Sb_{12}$ in this study.

Based on the authors' experiences with statistical DoE, we recommend the following steps when approaching an unfamiliar synthesis using statistical DoE as a guide. After a literature survey, the next step is a series of preliminary reactions guided by chemical intuition, just enough to find conditions in which the target compound can form. Next, one uses the knowledge acquired through the literature survey and preliminary reactions to choose factors for the DoE model. Permissible ranges for each factor are based on the results of preliminary reactions. The more factors there are in a model, the more trials are needed. By creating mock RSM DoE models in JMP software with various designs, we selected the one requiring the fewest data points, resulting in 16 reactions total. To ensure the resulting model is representative of the system in question, the reaction conditions must be attempted with the exact parameters suggested by the statistical software. After the model predicts optimal conditions, a batch of reactions at and near the predicted conditions should be attempted. If the predicted optimum does not produce the desired result, one must perform another iteration or choose different parameters to optimize. This will most likely entail removing unimportant

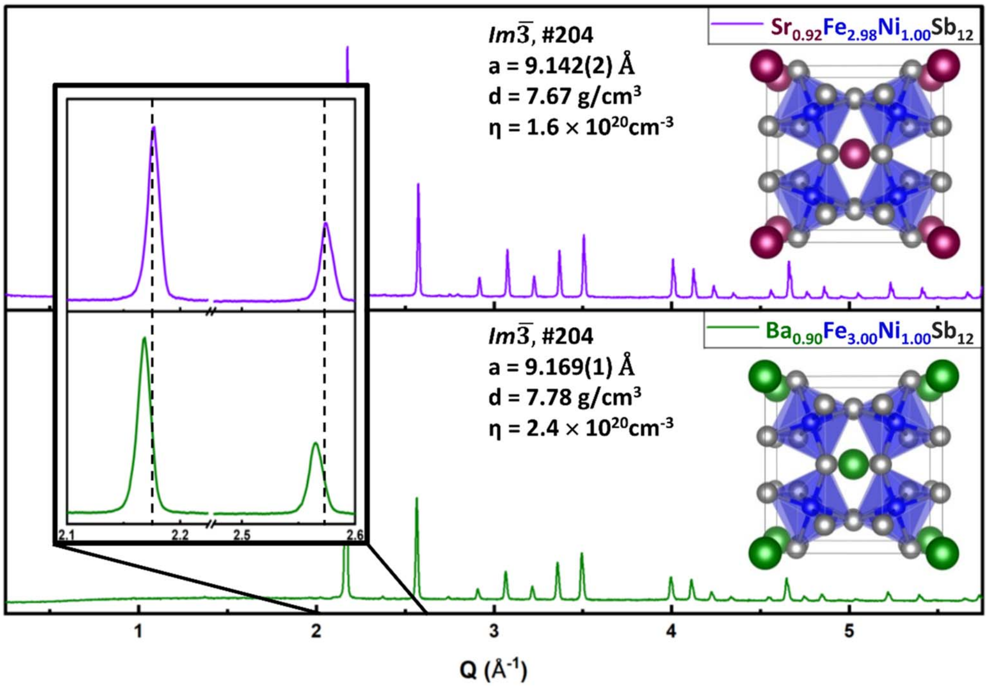

Fig. 7 Powder X-ray diffraction patterns of $SrFe_3NiSb_{12}$ and $BaFe_3NiSb_{12}$ with the crystal structure of the filled skutterudite structure type inset, and the shift in diffraction angle of the most intense Braggs' peaks corresponding to the filled skutterudite phase when filled with a different ion. General information pertaining to $SrFe_3NiSb_{12}$ and $BaFe_3NiSb_{12}$ is inset near the crystal structure. Cell parameters (*a*) are averaged from several replications at identical compositions. Theoretical densities (*d*) are calculated from cell volumes determined by Rietveld refinement and formula weights determined by EDXS stoichiometries. Carrier concentrations (*η*) are the averages of the carrier concentrations measured at 200 K, 250 K, and 300 K.

factors from the model, narrowing the range of values for some factor(s), or both.

Sometimes, the unimportance of certain aspects of synthesis can be exploited. In our case, the less important variables in the model of $Ba_{0.9}Fe_{3.00\pm x}Ni_{1.00\pm x}Sb_{12}$ and $Sr_{0.92}Fe_{2.98\pm x}Ni_{1.00\pm x}Sb_{12}$ were the exact loading stoichiometries of Fe and Ni. The ability to substitute Fe with Ni enabled us to tune the carrier concentrations (Fig. 7 and S8†) and improve thermoelectric performance.

Results of synthesis optimization

Synthesis and spark-plasma sintering (SPS) conditions were not universal within the $Ba_{0.9}Fe_{3.00\pm x}Ni_{1.00\pm x}Sb_{12}$ and $Sr_{0.92}Fe_{2.98\pm x}Ni_{1.00\pm x}Sb_{12}$ series of compounds, even though all are isostructural and have isovalent fillers (Note S1†). $Ba_{0.90}Fe_{3.00}Ni_{1.00}Sb_{12}$, $Ba_{0.90}Fe_{3.15}Ni_{0.85}Sb_{12}$ $Ba_{0.90}Fe_{3.30}Ni_{0.70}Sb_{12}$ were annealed at 855 K. More Ni-rich compositions $Ba_{0.85}Fe_{2.70}Ni_{1.30}Sb_{12}$ and $Ba_{0.85}Fe_{2.85}Ni_{1.15}Sb_{12}$, as well as the Sr-series were annealed at 893 K. Molar masses were determined by the loading stoichiometries of Fe and Ni and the EDXS-determined filling fractions of Ba or Sr (Table S1†). The Sr-series varied from 1757 g mol^{-1} to 1763 g mol^{-1} (0.3%), and the Ba-series varied from 1795 g mol^{-1} to 1812 g mol^{-1} (0.9%). Variations in molar mass were driven by changes in filling fraction because Sr and Ba are much heavier than Fe and Ni, and because the atomic weights of Fe and Ni are similar.

Crystallographic densities were calculated using the refined unit cell parameters (Fig. 7) of $Ba_{0.90}Fe_{3.00}Ni_{1.00}Sb_{12}$ for the Ba-series and $Sr_{0.92}Fe_{2.98}Ni_{1.00}Sb_{12}$ for the Sr-series. The compactness of pellets above 93% (Table S1 and Note S1†) of crystallographic density was achieved using individually tailored sintering conditions. The skutterudite phases were uniform in composition based on EDXS, although some SrO and BaO grains were seen at pellet surfaces (Fig. S9†) which resulted in scratches during polishing (Fig. S10†). Sintering results for pellets of all compositions (Table S1†) and backscattered electron micrographs (Fig. S9†) indicate that the pellets have similar microstructures and are compact enough for their transport properties to be directly comparable. Skutterudite grains in the SPS pellets are about 5 μm across and gain no obvious crystalline habit. Grain boundaries show little porosity and do not appear to contain precipitates.

EDXS measurements of transition metal stoichiometries are within one standard deviation of the stoichiometry used to make the sample in question. Skutterudites almost always have fractional occupancy of filler atoms.[11,12,27,28] EDXS suggests that the Sr-series have filling fractions of 80% (Table S1†), and the Ba series have filling fractions in the range of 76–90% that decrease when more Ni is added (Table S1†). The authors hypothesize that the Ba-series compensates for electron deficiency in the framework by accepting more electron-donating filler atoms into the structure. This variance in filling fraction with aliovalent doping of the skutterudite framework is also supported by the variation in SrH_2 and BaH_2 used to make pure skutterudites. Ni-enriched (hole deficient) $Ba_{0.85}Fe_{2.85}Ni_{1.15}Sb_{12}$ and $Ba_{0.85}Fe_{2.70}Ni_{1.30}Sb_{12}$ need only 0.85 instead of 0.90 equivalents of BaH_2 to minimize the phase fraction of $BaSb_3$ impurity in the reaction product. Ni-deficient (electron deficient) $Sr_{0.95}Fe_{3.43}Ni_{0.55}Sb_{12}$ is the only Sr-filled skutterudite herein that needs more than 0.92 equivalents of SrH_2 to minimize marcasite-type impurities (Note S2†).

Composition-dependent thermoelectric properties of $Ba_{0.9}Fe_{3.00\pm x}Ni_{1.00\pm x}Sb_{12}$ skutterudites

The values of resistivity, $\rho(T)$, for most $Ba_{0.9}Fe_{3.00\pm x}Ni_{1.00\pm x}Sb_{12}$ skutterudites are approximately 2 mΩ cm (Fig. 8A) and show weak temperature dependence, like the previous report of $Ba_{0.96}Fe_{3.0}Ni_{1.0}Sb_{12}$.[28] Therefore, they are "bad metals" or very heavily doped semiconductors, except $Ba_{0.85}Fe_{2.85}Ni_{1.15}Sb_{12}$. Its resistivity almost linearly decreases with temperature. $Ba_{0.85}Fe_{2.85}Ni_{1.15}Sb_{12}$ is the only skutterudite in the Ba-series to show semiconductor-like temperature dependence of resistivity, consistent with its VEC approaching 72 (0.8(2) + 2.85(8) + 1.15(10) + 12(3) = 71.9). Semiconductor-like electrical resistivity indicates that this skutterudite composition has a valence band filled to a level just below the band gap where the skutterudite structure affords a large density of states.[29,30] Changes to the Fe/Ni stoichiometry change the VEC, move the Fermi level, and cause the metallic behavior of the rest of the Ba-series.

Because of their similar VECs (Table S1†) and concomitant metallicity, the positive (p-type) Seebeck coefficients, $S(T)$, of $Ba_{0.90}Fe_{3.30}Ni_{0.70}Sb_{12}$, $Ba_{0.90}Fe_{3.15}Ni_{0.85}Sb_{12}$, and $Ba_{0.90}Fe_{3.00}Ni_{1.00}Sb_{12}$ reach maximum values between +135 and 150 μV K^{-1}. As shown in Fig. 8A and C, the semiconductor-like skutterudite in the series, $Ba_{0.85}Fe_{2.85}Ni_{1.15}Sb_{12}$, has a lower peak Seebeck coefficient of 87 μV K^{-1}. With a valence electron count of 72.3 (Table S1†), $Ba_{0.85}Fe_{2.70}Ni_{1.30}Sb_{12}$ is over-doped with Ni and displays n-type charge transport, indicated by its negative Seebeck coefficient. The magnitudes of the peak Seebeck coefficients observed for the Ba-filled skutterudites are limited by the

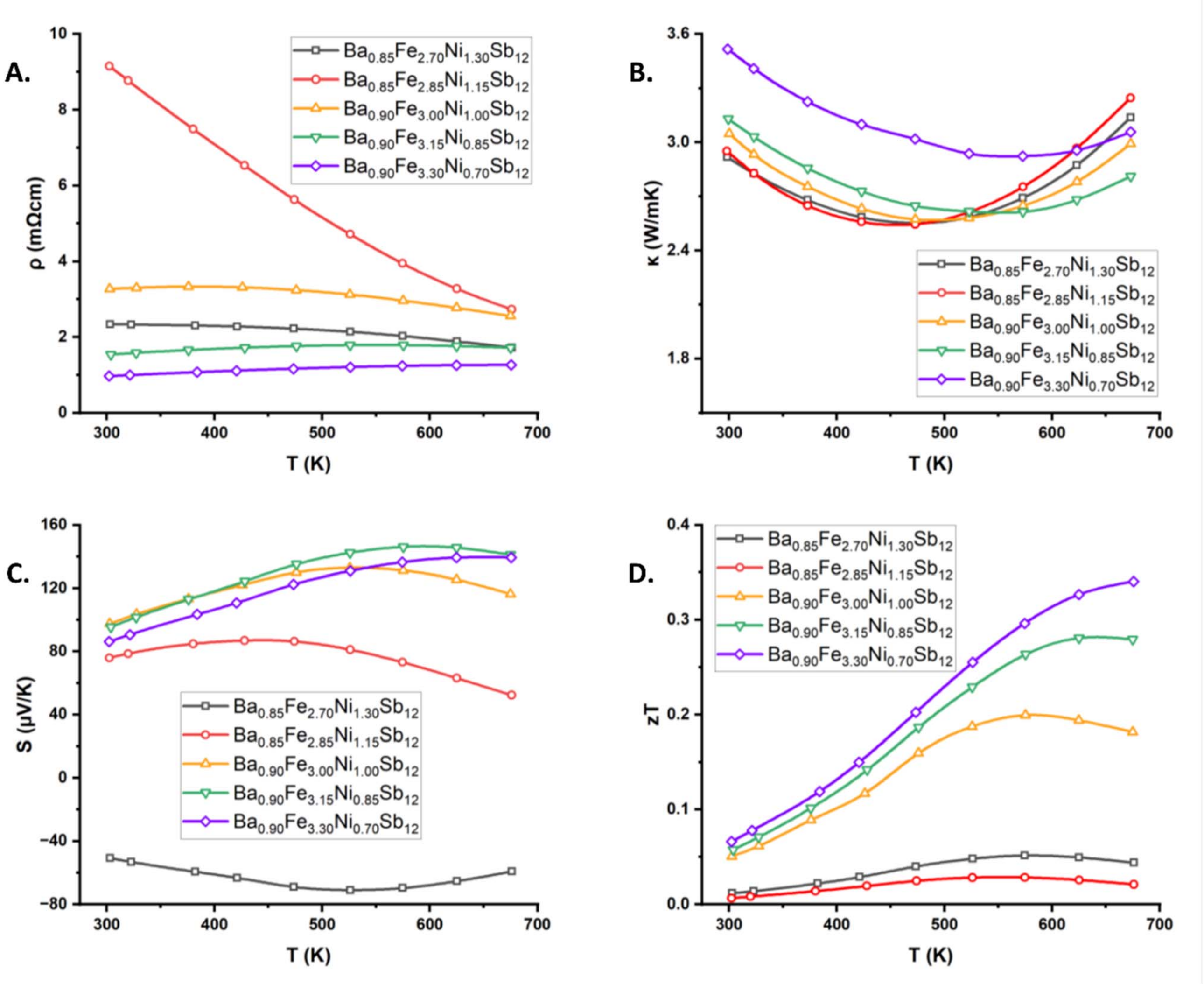

Fig. 8 Thermoelectric properties of the $Ba_{0.9}Fe_{3\pm x}Ni_{1\pm x}Sb_{12}$ skutterudites. (A) Electrical resistivities in milliohm-centimeters. (B) Thermal conductivities in watts per meter kelvin. (C) Seebeck coefficients in microvolts per kelvin. (D) Unitless figures of merit zT.

excitation of minority charge carriers. As temperature increases, electrons are excited into the conduction band in the p-type samples, as were holes in the n-type compound, resulting in bipolar charge transport. This is not unusual for thermoelectric materials measured near the top of their useful temperature range.

The skutterudites reported herein demonstrate bipolar conduction at temperatures lower than skutterudites made with Fe and Co that have the same VEC.[11] The extent of bipolar charge transport observed herein is consistent with the previous report of $Ba_{0.96}Fe_{3.0}Ni_{1.0}Sb_{12}$.[28] The values of the Seebeck coefficient at various temperatures are not directly comparable between that study[28] and this report. Here we used a Netzch Nemesis SBA, which measures the Seebeck coefficient without inducing a large thermal gradient across the sample. However, the previous report of $Ba_{0.96}Fe_{3.0}Ni_{1.0}Sb_{12}$ reports a Seebeck coefficient measured with an ULVAC-Rico ZEM-3 instrument, which has a different sample environment, resulting in a large temperature gradient across the sample and causing a pronounced cold-finger effect and significant overestimation of the Seebeck coefficient.[55] The temperature of the inflection points in the curves are comparable however, and quite similar. The highest peak Seebeck coefficient in the Ba-series herein belongs to a bad metal, not a heavily doped semiconductor. Therefore, the most important result of aliovalent doping in $Ba_{0.9}Fe_{3.00\pm x}Ni_{1.00\pm x}Sb_{12}$ is the suppression of bipolar charge transport. This is demonstrated by the two $Ba_{0.9}Fe_{3.00\pm x}Ni_{1.00\pm x}Sb_{12}$ with the best electronic transport performance. $Ba_{0.90}Fe_{3.15}Ni_{0.85}Sb_{12}$ had the highest peak Seebeck coefficient of the Ba-series with 146 $\mu V\ K^{-1}$ at 575 K despite its low VEC of 71.3. The onset temperature of bipolar charge transport is further increased for $Ba_{0.90}Fe_{3.30}Ni_{0.70}Sb_{12}$; its Seebeck coefficient plateaus at 675 K instead of 575 K like $Ba_{0.90}Fe_{3.15}Ni_{0.85}Sb_{12}$. Overall, increasing Ni content in our Fe–Ni skutterudites decreases the peak value of the Seebeck coefficient. Electrons from Ni cause excessive bipolar charge transport at lower VECs than would be expected for skutterudites made with a Fe–Co framework, as seen in literature.[11,49] Our results indicate that the optimal range of VECs for p-type Fe–Ni skutterudites is 71.0–71.5 rather than 71.5–72.0 as in Fe–Co skutterudites.

Thermal conductivities, $\kappa(T)$, are all similar for Ba-filled skutterudites (Fig. 8B), approximately 3 W mK^{-1}, consistent with the values previously reported[49] for $Ba_{0.96}Fe_{3.0}Ni_{1.0}Sb_{12}$. All values of thermal conductivity in the Ba-series are within experimental error except $Ba_{0.90}Fe_{3.30}Ni_{0.70}Sb_{12}$, which is more conductive near room temperature. All thermal conductivity curves also have similar shapes. One of the most noticeable differences between each curve is the position of the inflection point. In the p-type skutterudites pictured above, the temperature of the inflection points in $\kappa(T)$ increase as Fe content increases, which is attributed to the suppression of thermal conduction due to bipolar charge transport. The electronic contributions to thermal conductivities were calculated based on the Seebeck coefficients using Lorenz numbers calculated with the empirical equation proposed by Snyder *et al.*[56] The differences between total thermal conductivities above are also caused by electronic contributions to thermal conductivity, shown in Fig. S12A.† On average, the lattice thermal conductivity of the Ba-filled skutterudites discussed here is approximately 2.5 W mK^{-1}, which is common for singly filled skutterudites.[11] The lattice contribution to thermal conductivity is greater than the electronic component in all cases and accounts for roughly 3/4 of the total thermal conductivity. Electronic contributions to the total thermal conductivity of p-type samples show no trend with respect to Fe or Ni content or the valence electron count (Fig. S12A†).

Among our p-type $Ba_{0.9}Fe_{3.00\pm x}Ni_{1.00\pm x}Sb_{12}$ skutterudites, zT increased with Fe content. The highest zT of 0.34 is achieved by $Ba_{0.90}Fe_{3.30}Ni_{0.70}Sb_{12}$ at 675 K, and the temperature-dependence of zT did not plateau or decrease in the measured temperature range. The curves in Fig. 8D never cross over one another, so there is no temperature within the range tested in which $Ba_{0.90}Fe_{3.30}Ni_{0.70}Sb_{12}$ is not the highest-performing Ba-filled skutterudite in this study because it was the least encumbered by bipolar charge transport. However, further doping of Fe in place of Ni would not be productive for $Ba_{0.9}Fe_{3.00\pm x}Ni_{1.00\pm x}Sb_{12}$ skutterudites, as indicated by the similarities of the Seebeck coefficients of $Ba_{0.90}Fe_{3.15}Ni_{0.85}Sb_{12}$ and $Ba_{0.90}Fe_{3.30}Ni_{0.70}Sb_{12}$. More holes will not result in better thermoelectric performance, as shown by the carrier concentration of $Ba_{0.90}Fe_{3.30}Ni_{0.70}Sb_{12}$ (Fig. S8†), which exceeds $1.0 \times 10^{20}\ cm^{-3}$, the desirable carrier concentration in skutterudites.[11,15]

Composition-dependent thermoelectric properties in $Sr_{0.92}Fe_{2.98\pm x}Ni_{1.00\pm x}Sb_{12}$ skutterudites

The lowest electrical resistivities among the novel $Sr_{0.92}Fe_{2.98\pm x}Ni_{1.00\pm x}Sb_{12}$ series of skutterudites (0.5–3 mΩ cm) were generally like the Ba-series (1–4 m Ωcm). Most Sr-filled skutterudites are less resistive than their Ba-filled analogues (Fig. 9A) despite similar carrier concentrations (Fig. 7 and S8†). The three most Fe-rich $Sr_{0.92}Fe_{2.98\pm x}Ni_{1.00\pm x}Sb_{12}$ are bad metals. The Ni-rich skutterudites, $Sr_{0.92}Fe_{2.68}Ni_{1.30}Sb_{12}$ and $Sr_{0.92}Fe_{2.83}Ni_{1.15}Sb_{12}$, have VECs approaching 72 and show temperature dependence of electrical resistivity typical for heavily doped semiconductors. The 4 most Fe-rich $Sr_{0.92}Fe_{2.98\pm x}Ni_{1.00\pm x}Sb_{12}$ are p-type, with positive Seebeck coefficients. $Sr_{0.92}Fe_{2.68}Ni_{1.30}Sb_{12}$ is n-type with a negative Seebeck coefficient, like $Ba_{0.85}Fe_{2.70}Ni_{1.30}Sb_{12}$, but smaller in absolute value. The temperature dependence of the Seebeck coefficient $S(T)$ for Ni-rich $Sr_{0.92}Fe_{2.68}Ni_{1.30}Sb_{12}$ has an inflection point at 475 K, lower than 525 K for its Ba-analog, despite identical VECs between the compounds (Table S1†). The highest peak Seebeck coefficient of any material studied herein belongs to $Sr_{0.92}Fe_{2.98}Ni_{1.00}Sb_{12}$ (180 $\mu V\ K^{-1}$ at 575 K). Below 550 K (before excessive bipolar charge transport occurs), p-type $Sr_{0.92}Fe_{2.98\pm x}Ni_{1.00\pm x}Sb_{12}$ with more Ni have higher resistivities and higher Seebeck coefficients. In the Sr-series, $S(T)$ trends differently than the Ba-series, with the highest peak Seebeck coefficients seen in relatively Ni-rich samples at lower temperatures. However, higher resistivities make the *zTs* of $Sr_{0.92}Fe_{2.98}Ni_{1.00}Sb_{12}$ and $Sr_{0.92}Fe_{2.83}Ni_{1.15}Sb_{12}$ lower than $Sr_{0.92}Fe_{3.28}Ni_{0.70}Sb_{12}$ and $Sr_{0.92}Fe_{3.12}Ni_{0.85}Sb_{12}$. Therefore, to achieve maximum thermoelectric performance in $Sr_{0.92}Fe_{2.98\pm x}Ni_{1.00\pm x}Sb_{12}$ skutterudites,

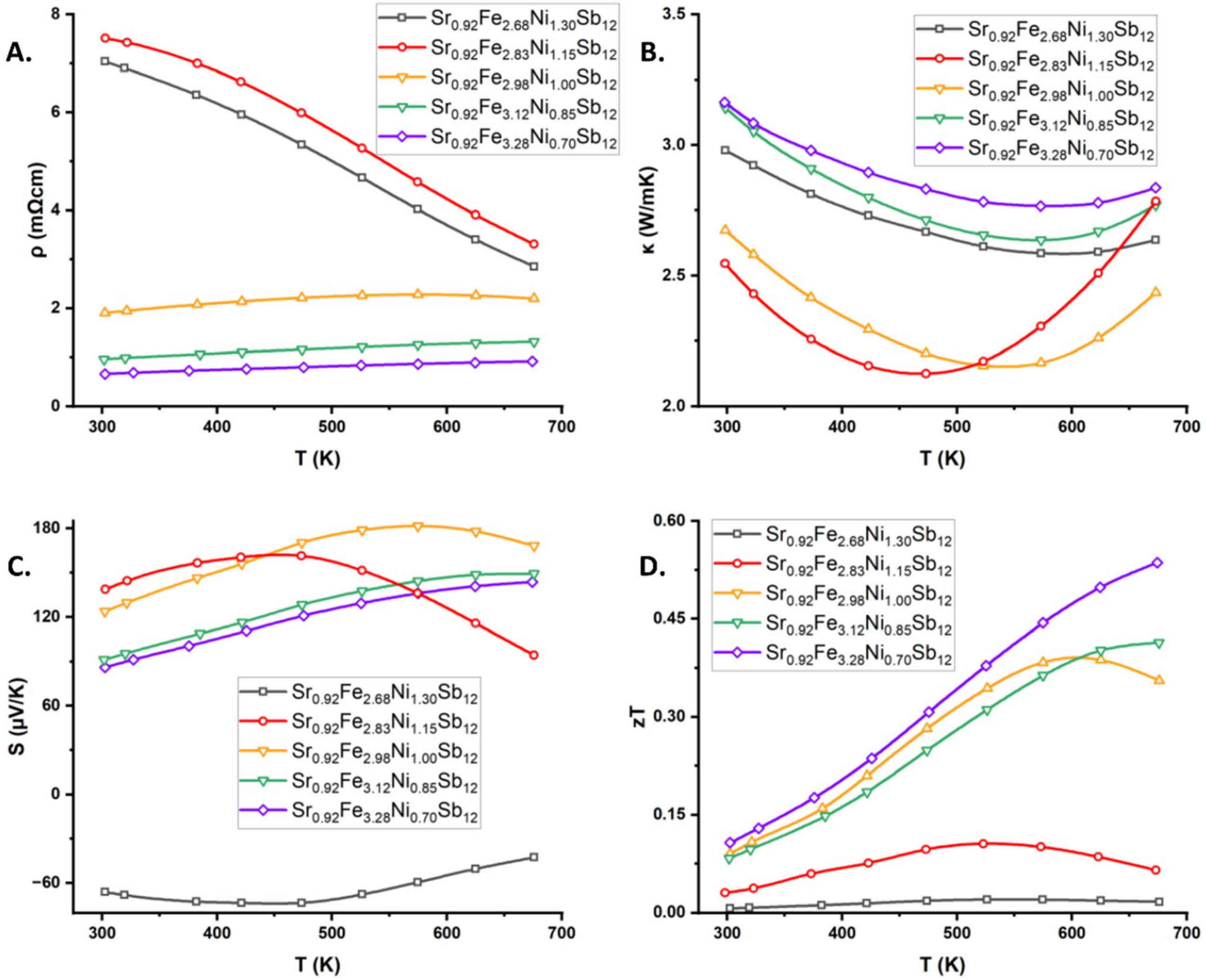

Fig. 9 Thermoelectric Properties of $Sr_{0.92}Fe_{2.98\pm x}Ni_{1\pm x}Sb_{12}$ skutterudites. (A) Electrical resistivities in milliohm-centimeters. (B) Thermal conductivities in watts per meter kelvin. (C) Seebeck coefficients in microvolts per kelvin. (D) Unitless figures of merit, *zT*.

suppressing bipolar charge transport is more important than maximizing the peak Seebeck coefficient.

Comparison of $Sr_{0.92}Fe_{2.98\pm x}Ni_{1.00\pm x}Sb_{12}$ and $Ba_{0.9}Fe_{3.00\pm x}Ni_{1.00\pm x}Sb_{12}$ reveals intriguing trends with regards to thermal conductivity. Like the Ba-series, p-type $Sr_{0.92}Fe_{2.98\pm x}Ni_{1.00\pm x}Sb_{12}$ skutterudites show inflection points in their $\kappa(T)$ curves (Fig. 9B). These inflection points also shift to higher temperatures as compositions get more Fe-rich and the bipolar contribution to thermal conductivity is minimized. Thermal conductivities for $Sr_{0.92}Fe_{2.98}Ni_{1.00}Sb_{12}$ and $Sr_{0.92}Fe_{2.83}Ni_{1.15}Sb_{12}$ are significantly lower than for the other skutterudites herein (≈ 2.5 W mK^{-1} at room temperature rather than ≈ 3.0 W mK^{-1}). Based on the lack of porosity in the sintered pellets observed by SEM (Fig. S11†) and the similarity between Archimedean and geometric densities of the pellets (Table S1†), low compactness of the sintered pellets is not the reason for their low thermal conductivity. Lattice and electronic contributions to total thermal conductivity (Fig. S12B†) just happen to be in a "sweet spot" for $Sr_{0.92}Fe_{2.98}Ni_{1.00}Sb_{12}$ and $Sr_{0.92}Fe_{2.83}Ni_{1.15}Sb_{12}$.

All the p-type skutterudites in the Sr-series have lattice thermal conductivities within experimental deviation of one another (Fig. S12†). Overall, the lattice contributions to thermal conductivity are smaller in the Sr-series (≈ 2.4 W mK^{-1}) than in the Ba-series (≈ 2.8 W mK^{-1}). The electronic contributions to thermal conductivity decrease with Ni content across the Sr-series as one would expect when electron-doping a p-type bad metal (Fig. S12A†). The electronic and lattice contributions to the thermal conductivity of $Sr_{0.92}Fe_{3.28}Ni_{0.70}Sb_{12}$ become very similar (≈ 1.3 W mK^{-1} and ≈ 1.6 W mK^{-1} respectively) at 675 K, which is unusual for skutterudites, which typically have larger lattice contributions to the total thermal conductivity.

Like the Ba-series, peak thermoelectric figures of merit (*zT*) for the Sr-filled iron–nickel skutterudites increase with decreasing Ni content until $Sr_{0.92}Fe_{3.28}Ni_{0.70}Sb_{12}$, which has a peak *zT* of 0.54 at 673 K. We note that using values of thermal conductivity determined experimentally by reference to a pyroceram standard pellet results in a lower thermal conductivity, and a peak zT of 0.66 at 673 K ($\kappa_{\text{experimental}} \approx 2.3$ W mK^{-1}). However, the temperature dependence of the experimentally determined thermal conductivity (Fig. S13†) fluctuates considerably due to variations in the experimentally determined heat capacity of the sample.

$Sr_{0.92}Fe_{3.28}Ni_{0.70}Sb_{12}$ has the highest zT of the materials reported herein, with the next highest being $Sr_{0.92}Fe_{3.12}Ni_{0.85}Sb_{12}$ and $Sr_{0.92}Fe_{2.98}NiSb_{12}$. Further decreasing Ni stoichiometry does not increase zT. The differences in values and curve shapes between $Sr_{0.92}Fe_{3.28}Ni_{0.70}Sb_{12}$ and $Sr_{0.92}Fe_{3.12}Ni_{0.85}Sb_{12}$ in Fig. 9 were minimal except Fig. 9D. Lower Ni content results in excessive hole concentrations, and therefore, decreased thermoelectric performance. The carrier concentration of $Sr_{0.92}Fe_{3.28}Ni_{0.70}Sb_{12}$ already exceeds 1.0×10^{20} per cm^3 (Fig. S8†), the preferred[11] carrier concentration in thermoelectric skutterudites.

$Sr_{0.95}Fe_{3.43}Ni_{0.55}Sb_{12}$ (made as a proof-of-concept) has a smaller Seebeck coefficient than $Sr_{0.92}Fe_{3.28}Ni_{0.70}Sb_{12}$ (Fig. S14†). The increased resistivity of $Sr_{0.95}Fe_{3.43}Ni_{0.55}Sb_{12}$ as compared with $Sr_{0.92}Fe_{3.28}Ni_{0.70}Sb_{12}$ is likely a result of poor compaction caused by the poor stability of $Sr_{0.95}Fe_{3.43}Ni_{0.55}Sb_{12}$ during sintering. However, even if $Sr_{0.95}Fe_{3.43}Ni_{0.55}Sb_{12}$ had the same resistivity as $Sr_{0.92}Fe_{3.28}Ni_{0.70}Sb_{12}$, its lower Seebeck coefficient would result in a lower zT. The previous report of $SrFe_4Sb_{12}$ reinforces this point. The resistivity and Seebeck coefficient of $SrFe_4Sb_{12}$[57] were smaller than $Sr_{0.92}Fe_{3.28}Ni_{0.70}Sb_{12}$. Other literature also shows that doping of Fe–Ni skutterudites results in maximum zT values across a series of compositions when the VEC is between 71 and 72,[13–15,25,26,58] not 70 as in $SrFe_4Sb_{12}$. Based on thermoelectric properties observed in this study and prior literature, future p-type Fe–Ni skutterudites should target a VEC in the range 71.0–71.5 and prefer Sr-filling over Ba-filling.

Conclusions

Thermoelectric skutterudites $Sr_{0.92}Fe_{2.98\pm x}Ni_{1.00\pm x}Sb_{12}$ and $Ba_{0.9}Fe_{3.00\pm x}Ni_{1.00\pm x}Sb_{12}$ were synthesized using the hydride route. Easy mixing and relatively low reaction temperatures enabled by the reactivity and fine particle size of BaH_2 and SrH_2 precursors allowed the use of statistical analysis tools for design of experiments (DoE) to optimize synthetic conditions. High-temperature *in situ* synchrotron powder X-ray diffraction revealed that $BaFe_3NiSb_{12}$ forms from a reaction between elemental Sb, binary barium antimonides, and binary Fe and Ni antimonides at 855 K. The optimal synthesis temperature for $Ba_{0.90}Fe_{3.00}Ni_{1.00}Sb_{12}$ in the lab on the 0.5 g and 2.2 g scales was 855 K. By directly observing the synthesis process, it was possible to pinpoint the synthesis temperature directly. The statistical model of $Ba_{0.90}Fe_{3.00}Ni_{1.00}Sb_{12}$ synthesis provided proof-of-concept, validating the application of statistical analysis software to solid-state reactions in multinary phase space. Phase fraction variations determined by laboratory powder X-ray diffraction were used to judge the effects of altered synthesis conditions by parameterizing variations in stoichiometry and annealing temperature. The applicability of statistical DoE tools for hydride synthesis was further established for the synthesis of $Sr_{0.92}Fe_{2.98}Ni_{1.00}Sb_{12}$. This optimization resulted in synthesis conditions that yielded high-purity samples with variable Fe–Ni content. Our efforts demonstrate that complex solid-state phase spaces can be analyzed and explored efficiently using statistical design of experiment methods. Statistical analyses of the syntheses of $Sr_{0.92}Fe_{2.98\pm x}Ni_{1.00\pm x}Sb_{12}$ and $Ba_{0.9}Fe_{3.00\pm x}Ni_{1.00\pm x}$ demonstrated that the formation of these skutterudites is nearly independent of Fe and Ni stoichiometry between the compositions (Sr/Ba)$Fe_{3.30}Ni_{0.70}Sb_{12}$ and (Sr/Ba)$Fe_{2.70}Ni_{1.30}Sb_{12}$. Nickel-containing skutterudites were found to have a significant bipolar contribution to their electronic transport properties, consistent with previous literature. Using the exchange of Fe atoms with Ni atoms as a means of electron doping enabled the tuning of electronic transport properties, resulting in a measured peak zT of 0.54 at 673 K for the skutterudite $Sr_{0.92}Fe_{3.28}Ni_{0.70}Sb_{12}$.

Data availability

The data supporting this article have been included in the ESI† and manuscript figures.

Author contributions

Zaikina Julia V: project administration, supervision, methodology, funding acquisition, data curation, writing – review and editing. Rae Earnest: validation, data curation, formal analysis. Thomas A. Seymour-Cozzini: validation, data curation, formal analysis, supervision, writing – original draft.

Conflicts of interest

The authors have no conflicts to declare.

Acknowledgements

The authors wish to thank Dr Tori Cox, Kaden Osborn and Bradyn Weaver for assistance with sample preparation, Dr Arka Sarkar for PPMS measurements, and William Cozzini for editorial assistance. Financial support from the National Science Foundation (U.S.) Division of Materials Research (DMR-1944551) CAREER Award is gratefully acknowledged. T. S–C. and J. V. Z. acknowledge financial support from the LAS Frontier Science Fund established by Iowa State University alumni and donors Tom and Evonne Smith. We are grateful to the staff at the Advanced Photon Source, Argonne National Lab, Dr Wenquian Xu, especially, for assistance in planning experiments and configuring equipment for high-temperature *in situ* powder X-ray diffraction at sector 17-BM. This research was performed on APS beam time award (experiment no. 258750) from the Advanced Photon Source, a U.S. Department of Energy (DOE) Office of Science user facility operated for the DOE Office of Science by Argonne National Laboratory under Contract No. DE-AC02-06CH11357. Parts of the TOC figure were generated using

AI tools (Google Gemini) and subsequently edited by the authors.

References

1 *Energy Flow Charts*, Lawrence Livermore National Laboratory and United States Department of Energy, 2022.

2 D. Beretta, N. Neophytou, J. M. Hodges, M. G. Kanatzidis, D. Narducci, M. Martin-Gonzalez, M. Beekman, B. Balke, G. Cerretti, W. Tremel, A. Zevalkink, A. I. Hofmann, C. Müller, B. Dörling, M. Campoy-Quiles and M. Caironi, Thermoelectrics: From History, a Window to the Future, *Mater. Sci. Eng., R*, 2019, **138**, 100501, DOI: 10.1016/j.mser.2018.09.001.

3 R. L. McNutt, R. F. Wimmer-Schweingruber, M. Gruntman, S. M. Krimigis, E. C. Roelof, P. C. Brandt, S. R. Vernon, M. V. Paul, B. W. Lathrop, D. S. Mehoke, D. H. Napolillo and R. W. Stough, Near-Term Interstellar Probe: First Step, *Acta Astronaut.*, 2019, **162**, 284–299, DOI: 10.1016/j.actaastro.2019.06.013.

4 A. F. Ioffe, L. S. Stil'bans, E. K. Iordanishvili, T. S. Stavitskaya, *Semiconductor Thermoelements and Thermoelectric Cooling*, ed. H. J. Goldsmid, 1957.

5 M. Beekman, D. T. Morelli and G. S. Nolas, Better Thermoelectrics through Glass-like Crystals, *Nat. Mater.*, 2015, **14**, 1182–1185.

6 H. J. Wu, L. D. Zhao, F. S. Zheng, D. Wu, Y. L. Pei, X. Tong, M. G. Kanatzidis and J. Q. He, Broad Temperature Plateau for Thermoelectric Figure of Merit ZT>2 in Phase-Separated $PbTe_{0.7}S_{0.3}$, *Nat. Commun.*, 2014, **5**(4515), DOI: 10.1038/ncomms5515.

7 C. B. Vining, An Inconvenient Truth about Thermoelectrics, 2009, www.sc.doe.gov/bes/reports/abstracts.html#SEU.

8 G. A. Slack, New Materials and Performance Limits for Thermoelectric Cooling, in *CRC Handbook on Thermoelectric Materials*, ed. Rowe, D. M., CRC Press, 1995, pp. 407–437.

9 A. Kjekshus and T. Rakke, Compounds with the Skutterudite Type Crystal Structure III. Structure Data for Arsenides and Antimonides, *Acta Chem. Scand., Ser. A*, 1974, **28**, 99–103.

10 D. J. Braun and W. Jeitschko, Preparation and structural investigations of antimonides with the $LaFe_4P_{12}$ structure, *J. Less-Common Met.*, 1980, **72**(1), 147–156.

11 R. Freer, D. Ekren, T. Ghosh, K. Biswas, P. Qiu, S. Wan, L. Chen, S. Han, C. Fu, T. Zhu, A. K. M. Ashiquzzaman Shawon, A. Zevalkink, K. Imasato, G. J. Snyder, M. Ozen, K. Saglik, U. Aydemir, R. Cardoso-Gil, E. Svanidze, R. Funahashi, A. V. Powell, S. Mukherjee, S. Tippireddy, P. Vaqueiro, F. Gascoin, T. Kyratsi, P. Sauerschnig and T. Mori, Key Properties of Inorganic Thermoelectric Materials - Tables (Version 1), *J. Phys. Energy*, 2022, **4**(2), 20–32, DOI: 10.1088/2515-7655/ac49dc.

12 M. Rull-Bravo, A. Moure, J. F. Fernández and M. Martín-González, Skutterudites as Thermoelectric Materials: Revisited, *RSC Adv.*, 2015, 41653–41667, DOI: 10.1039/c5ra03942h.

13 G. Rogl, A. Grytsiv, E. Bauer, P. Rogl and M. Zehetbauer, Thermoelectric Properties of Novel Skutterudites with Didymium: $DD_y(Fe_{1-X}Co_x)_4Sb_{12}$ and $DD_y(Fe_{1-X}Ni_x)_4Sb_{12}$, *Intermetallics*, 2010, **18**(1), 57–64, DOI: 10.1016/j.intermet.2009.06.005.

14 T. Dahal, Q. Jie, Y. Lan, C. Guo and Z. Ren, Thermoelectric Performance of Ni Compensated Cerium and Neodymium Double Filled P-Type Skutterudites, *Phys. Chem. Chem. Phys.*, 2014, **16**(34), 18170–18175, DOI: 10.1039/c4cp00383g.

15 L. Fu, Q. Jiang, J. Yang, J. Peng, Y. Xiao, Y. Luo, Z. Zhou and D. Zhang, Enhancement of Thermoelectric Properties of $Ce_{0.9}Fe_{3.75}Ni_{0.25}Sb_{12}$ p-Type Skutterudite by Tellurium Addition, *J. Mater. Chem. A*, 2016, **4**(42), 16499–16506, DOI: 10.1039/c6ta06325j.

16 G. J. Miller, M. W. Schmidt, T.-S. You, F. Wang, Quantitative Advances in the Zintl-Klemm Formalism, in *Zintl Phases: Principles and Recent Developments*, 2011, vol 139, pp. 1–55.

17 *Chemistry, Structure, and Bonding of Zintl Phases and Ions*, ed. Kauzlarich, S. M., VCH Publishers, Inc., New York, 1996.

18 A. Kjekshus, D. G. Nicholson and T. Rakke, Compounds with the Skutterudite Type Crystal Structure II.121Sb Mossbauer Effect n $CoSb_3$, $Fe_{0.5}Ni_{0.5}Sb_3$, $RhSb_3$, and $IrSb_3$, *Acta Chem. Scand.*, 1973, **27**, 1315–1320.

19 E. M. Williamson and R. L. Brutchey, Using Data-Driven Learning to Predict and Control the Outcomes of Inorganic Materials Synthesis, *Inorg. Chem.*, 2023, **62**(40), 16251–16262, DOI: 10.1021/acs.inorgchem.3c02697.

20 E. J. Braham, R. D. Davidson, M. Al-Hashimi, R. Arróyave and S. Banerjee, Navigating the Design Space of Inorganic Materials Synthesis Using Statistical Methods and Machine Learning, *Dalton Trans.*, 2020, **49**(33), 11480–11488, DOI: 10.1039/d0dt02028a.

21 L. R. Karadaghi, M. S. Madani, E. M. Williamson, A. T. To, S. E. Habas, F. G. Baddour, J. A. Schaidle, D. A. Ruddy, R. L. Brutchey and N. Malmstadt, Throughput Optimization of Molybdenum Carbide Nanoparticle Catalysts in a Continuous Flow Reactor Using Design of Experiments, *ACS Appl. Nano Mater.*, 2022, **5**(2), 1966–1975, DOI: 10.1021/acsanm.1c02916.

22 J. Mingear, B. Zhang, D. Hartl and A. Elwany, Effect of Process Parameters and Electropolishing on the Surface Roughness of Interior Channels in Additively Manufactured Nickel-Titanium Shape Memory Alloy Actuators, *Addit. Manuf.*, 2019, **27**, 565–575, DOI: 10.1016/j.addma.2019.03.027.

23 A. Solomou, G. Zhao, S. Boluki, J. K. Joy, X. Qian, I. Karaman, R. Arróyave and D. C. Lagoudas, Multi-Objective Bayesian Materials Discovery: Application on the Discovery of Precipitation Strengthened NiTi Shape Memory Alloys through Micromechanical Modeling, *Mater. Des.*, 2018, **160**, 810–827, DOI: 10.1016/j.matdes.2018.10.014.

24 D. Xue, D. Xue, R. Yuan, Y. Zhou, P. V. Balachandran, X. Ding, J. Sun and T. Lookman, An Informatics Approach to Transformation Temperatures of NiTi-Based Shape Memory Alloys, *Acta Mater.*, 2017, **125**, 532–541, DOI: 10.1016/j.actamat.2016.12.009.

25 P. F. Qiu, R. H. Liu, J. Yang, X. Shi, X. Y. Huang, W. Zhang, L. D. Chen, J. Yang and D. J. Singh, Thermoelectric Properties of Ni-Doped $CeFe_4Sb_{12}$ Skutterudites, *J. Appl. Phys.*, 2012, **111**(2), 023705, DOI: **10.1063/1.3677971**.

26 J. Y. Cho, Z. Ye, M. M. Tessema, R. A. Waldo, J. R. Salvador, J. Yang, W. Cai and H. Wang, Thermoelectric Properties of P-Type Skutterudites $Yb_XFe_{3.5}Ni_{0.5}Sb_{12}$ ($0.8 \leq x \leq 1$), *Acta Mater.*, 2012, **60**(5), 2104–2110, DOI: **10.1016/j.actamat.2011.12.022**.

27 L. Chen, X. Tang, T. Goto and T. Hirai, Synthesis of Filled Skutterudite Compounds: $Ba_yFe_xCo_{4-X}Sb_{12}$, *J. Mater. Res.*, 2000, **15**(11), 2276–2279, DOI: **10.1557/JMR.2000.0325**.

28 G. Rogl, A. Grytsiv, P. Rogl, E. Bauer and M. Zehetbauer, A New Generation of P-Type Didymium Skutterudites with High ZT, *Intermetallics*, 2011, **19**(4), 546–555, DOI: **10.1016/j.intermet.2010.12.001**.

29 A. Leithe-Jasper, W. Schnelle, H. Rosner, M. Baenitz, A. Rabis, A. A. Gippius, E. N. Morozova, H. Borrmann, U. Burkhardt, R. Ramlau, U. Schwarz, J. A. Mydosh, Y. Grin, V. Ksenofontov and S. Reiman, Weak Itinerant Ferromagnetism and Electronic and Crystal Structures of Alkali-Metal Iron Antimonides: $NaFe_4Sb_{12}$ and KFe_4Sb_{12}, *Phys. Rev. B: Condens. Matter Mater. Phys.*, 2004, **70**(21), 214418, DOI: **10.1103/PhysRevB.70.214418**.

30 G. Sheet, H. Rosner, S. Wirth, A. Leithe-Jasper, W. Schnelle, U. Burkhardt, J. A. Mydosh, P. Raychaudhuri and Y. Grin, High Spin Polarization in the Ferromagnetic Filled Skutterudites KFe_4Sb_{12} and $NaFe_4Sb_{12}$, *Phys. Rev. B: Condens. Matter Mater. Phys.*, 2005, **72**(18), 180407, DOI: **10.1103/PhysRevB.72.180407**.

31 P. M. Murray, F. Bellany, L. Benhamou, D. K. Bučar, A. B. Tabor and T. D. Sheppard, The Application of Design of Experiments (DoE) Reaction Optimisation and Solvent Selection in the Development of New Synthetic Chemistry, *Org. Biomol. Chem.*, 2016, **14**, 2373–2384, DOI: **10.1039/c5ob01892g**.

32 G. D. Bowden, B. J. Pichler and A. Maurer, A Design of Experiments (DoE) Approach Accelerates the Optimization of Copper-Mediated 18F-Fluorination Reactions of Arylstannanes, *Sci. Rep.*, 2019, **9**(1), 11370, DOI: **10.1038/s41598-019-47846-6**.

33 D. D. Youmans, H. N. Tran and L. M. Stanley, Nickel-Catalyzed Isomerization of Homoallylic Alcohols, *Org. Lett.*, 2023, **25**(19), 3559–3563, DOI: **10.1021/acs.orglett.3c01201**.

34 S. E. Denmark and C. R. Butler, Vinylation of Aromatic Halides Using Inexpensive Organosilicon Reagents. Illustration of Design of Experiment Protocols, *J. Am. Chem. Soc.*, 2008, **130**(11), 3690–3704, DOI: **10.1021/ja7100888**.

35 E. M. Williamson, Z. Sun, L. Mora-Tamez and R. L. Brutchey, Design of Experiments for Nanocrystal Syntheses: A How-To Guide for Proper Implementation, *Chem. Mater.*, 2022, **34**(22), 9823–9835, DOI: **10.1021/acs.chemmater.2c02924**.

36 J.-H. Pöhls, C.-W. T. Lo, M. MacIver, Y.-C. Tseng and Y. Mozharivskyj, Driving Thermoelectric Optimization in $AgSbTe_2$ via Design of Experiments and Machine Learning, *Chem. Mater.*, 2025, **37**(6), 2281–2289, DOI: **10.1021/acs.chemmater.5c00022**.

37 Match! - Phase Analysis using Powder Diffraction, *Crystal Impact - Dr. H. Putz & Dr. K. Brandenburg GbR, Kreuzherrenstr.*, **102**, 53227 Bonn, Germany, **https://www.crystalimpact.de/match**.

38 B. H. Toby and R. B. Von Dreele, The Genesis of a Modern Open-Source All Purpose Crystallography Software Package, *J. Appl. Crystallogr.*, 2013, **46**(2), 544–549, DOI: **10.1107/S0021889813003531**.

39 P. J. Chupas, K. W. Chapman, C. Kurtz, J. C. Hanson, P. L. Lee and C. P. Grey, A Versatile Sample-Environment Cell for Non-Ambient X-Ray Scattering Experiments, *J. Appl. Crystallogr.*, 2008, **41**(4), 822–824, DOI: **10.1107/S0021889808020165**.

40 R. K. Meyer and C. J. Nachtsheim, The Coordinate-Exchange Algorithm for Constructing Exact Optimal Experimental Designs, *Technometrics*, 1995, **37**(1), 60–69.

41 P. Goos and B. Jones, *Optimal Design of Experiments a Case Study Approach*, Wiley, 2011.

42 A. N. Adeyemi, G. Bhaskar, T. Cox, S. Hong, V. Gvozdetskyi and J. V. Zaikina, Hydride Precursors in Materials Synthesis, in *Comprehensive Inorganic Chemistry III* Third Edition, Elsevier, 2023, vol. 1–10, pp. 128–146, DOI: **10.1016/B978-0-12-823144-9.00149-7**.

43 V. Gvozdetskyi, S. J. Lee, B. Owens-Baird, J. A. Dolyniuk, T. Cox, R. Wang, Z. Lin, K. M. Ho and J. V. Zaikina, Ternary Zinc Antimonides Unlocked Using Hydride Synthesis, *Inorg. Chem.*, 2021, **60**(14), 10686–10697, DOI: **10.1021/acs.inorgchem.1c01381**.

44 A. Mantravadi, V. Gvozdetskyi, A. Sarkar, Y. Mudryk and J. V. Zaikina, Exploring the A-V-Sb Landscape beyond AV_3Sb_5: A Case Study on the KV_6Sb_6 Kagome Compound, *Phys. Rev. Mater.*, 2023, **7**(11), 115002, DOI: **10.1103/PhysRevMaterials.7.115002**.

45 T. Cox, V. Gvozdetskyi, B. Owens-Baird and J. V. Zaikina, Rapid Phase Screening via Hydride Route: A Discovery of $K_{8-x}Zn_{18+3x}Sb_{16}$, *Chem. Mater.*, 2018, **30**(23), 8707–8715, DOI: **10.1021/acs.chemmater.8b04211**.

46 V. Gvozdetskyi, B. Owens-Baird, S. Hong and J. V. Zaikina, Thermal Stability and Thermoelectric Properties of NaZnSb, *Materials*, 2018, **12**(1), 48, DOI: **10.3390/ma12010048**.

47 J. V. Zaikina, M. Batuk, A. M. Abakumov, A. Navrotsky and S. M. Kauzlarich, Facile Synthesis of $Ba_{1-x}K_xFe_2As_2$ Superconductors via Hydride Route, *J. Am. Chem. Soc.*, 2014, **136**(48), 16932–16939, DOI: **10.1021/ja509907r**.

48 J. V. Zaikina, M. Y. Kwong, B. Baccam and S. M. Kauzlarich, Superconductor-in-an-Hour: Spark Plasma Synthesis of Co- and Ni-Doped $BaFe_2As_2$, *Chem. Mater.*, 2018, **30**(24), 8883–8890, DOI: **10.1021/acs.chemmater.8b04039**.

49 R. Liu, J. Y. Cho, J. Yang, W. Zhang and L. Chen, Thermoelectric Transport Properties of $R_yFe_3NiSb_{12}$ (R=Ba, Nd and Yb), *J. Mater. Sci. Nanotechnol.*, 2014, **30**(11), 1134–1140, DOI: **10.1016/j.jmst.2014.05.007**.

50 A. Kjekshus, T. Rakke and A. F. Andresen, Compounds with the Marcasite Type Crystal Structure. IX. Structural Data for

$FeAs_2$, $FeSe_2$, $NiAs_2$, $NiSb_2$, and $CuSe_2$, *Acta Chem. Scand.*, 1974, **28**, 996–1000.

51 A. Kjekshus and T. Rakke, Compounds with the Marcasite Type Crystal Structure. X. ^{57}Fe Mossbauer Studies of Some Ternary Pnictides, *Acta Chem. Scand.*, 1974, **28**, 1001–1010.

52 S. Ghosh, R. Seede, J. James, I. Karaman, A. Elwany, D. Allaire and R. Arroyave, Statistical Modelling of Microsegregation in Laser Powder-Bed Fusion, *Philos. Mag. Lett.*, 2020, **100**(6), 271–282, DOI: **10.1080/09500839.2020.1753894**.

53 S. Greenland, S. J. Senn, K. J. Rothman, J. B. Carlin, C. Poole, S. N. Goodman and D. G. Altman, Statistical tests, P values, confidence intervals, and power: a guide to misinterpretations, *Eur J Epidemiol.*, 2016, **31**(4), 337–350, DOI: **10.1007/s10654-016-0149-3**.

54 *NIST Engineering Statistics Handbook Chapter 5. Process Improvement*, **https://www.itl.nist.gov/div898/handbook/pri/pri.htm**.

55 K. A. Borup, J. De Boor, H. Wang, F. Drymiotis, F. Gascoin, X. Shi, L. Chen, M. I. Fedorov, E. Müller, B. B. Iversen and G. J. Snyder, Measuring Thermoelectric Transport Properties of Materials, *Energy Environ Sci.*, 2015, **1**, 423–435, DOI: **10.1039/c4ee01320d**.

56 H. S. Kim, Z. M. Gibbs, Y. Tang, H. Wang and G. J. Snyder, Characterization of Lorenz Number with Seebeck Coefficient Measurement, *APL Mater.*, 2015, **3**(4), 041506, DOI: **10.1063/1.4908244**.

57 P. F. Qiu, J. Yang, R. H. Liu, X. Shi, X. Y. Huang, G. J. Snyder, W. Zhang and L. D. Chen, High-Temperature Electrical and Thermal Transport Properties of Fully Filled Skutterudites RFe_4Sb_{12} (R= Ca, Sr, Ba, La, Ce, Pr, Nd, Eu, and Yb), *J. Appl. Phys.*, 2011, **109**(6), 063713, DOI: **10.1063/1.3553842**.

58 G. Tan, S. Wang, Y. Yan, H. Li and X. Tang, Enhanced Thermoelectric Performance in P-Type $Ca_{0.5}Ce_{0.5}Fe_{4-x}Ni_xSb_{12}$ Skutterudites by Adjusting the Carrier Concentration, *J. Alloys Compd.*, 2012, **513**, 328–333, DOI: **10.1016/j.jallcom.2011.10.042**.